



Published in final edited form as:

Nat Cancer. 2022 May ; 3(5): 595–613. doi:10.1038/s43018-022-00366-1.

IKAROS and MENIN Coordinate Therapeutically Actionable Leukaemogenic Gene Expression in MLL-r Acute Myeloid Leukaemia

Brandon J. Aubrey^{1,2,14}, Jevon A. Cutler^{1,14}, Wallace Bourgeois^{1,3,14}, Katherine A. Donovan^{4,5}, Shengqing Gu^{6,7}, Charlie Hatton¹, Sarah Perlee¹, Florian Perner^{1,8}, Homa Rahnamoun¹, Alexandra C. P. Theall¹, Jill A. Henrich¹, Qian Zhu^{1,3}, Radosław P. Nowak^{4,5}, Young Joon Kim¹, Salma Parvin⁹, Anjali Cremer^{1,10,11}, Sarah Naomi Olsen¹, Nicholas A. Eleuteri⁴, Yana Pikman^{1,3}, Gerard M. McGeehan¹², Kimberly Stegmaier^{1,3,13}, Anthony Letai⁹, Eric S. Fischer^{4,5}, X. Shirley Liu^{6,7}, Scott A. Armstrong^{1,3,*}

¹Department of Pediatric Oncology, Dana-Farber Cancer Institute, Boston, MA, 02215, USA

²Department of Medicine, Massachusetts General Hospital, Boston, MA, 02215, USA

³Division of Hematology-Oncology, Boston Children's Hospital, Boston, MA, 02115, USA

⁴Department of Cancer Biology, Dana-Farber Cancer Institute, Boston, MA, 02215, USA

⁵Department of Biological Chemistry and Molecular Pharmacology, Harvard Medical School, Boston, MA, 02115, USA

⁶Department of Data Science, Dana-Farber Cancer Institute, Boston, MA, 02215, USA

⁷Center for Functional Cancer Epigenetics, Dana-Farber Cancer Institute, Boston, MA, 02215, USA

⁸Internal Medicine C, Universitaetsmedizin Greifswald, Greifswald, 17489, Germany

⁹Department of Medical Oncology, Dana-Farber Cancer Institute, Boston, MA, 02215, USA

¹⁰University Hospital Frankfurt, Department of Hematology/Oncology, Frankfurt/Main, Germany

¹¹German Cancer Consortium, German Cancer Research Center, Heidelberg, 69120, Germany

¹²Syndax Pharmaceuticals, Waltham, MA, 02451, USA

¹³The Broad Institute of MIT and Harvard, Cambridge, MA, 02142, USA

¹⁴These authors contributed equally

Abstract

Users may view, print, copy, and download text and data-mine the content in such documents, for the purposes of academic research, subject always to the full Conditions of use:http://www.nature.com/authors/editorial_policies/license.html#terms

*Correspondence: scott_armstrong@dfci.harvard.edu.

Author Contributions

S.A.A supervised the study. S.A.A., B.J.A., J.A.C., W.B. conceived the study and performed data analysis. C.H. and Q.Z. performed bioinformatics analysis. B.J.A., J.A.C., W.B., R.P.N. S.Pa and K.A.D. performed experiments. A.C.P.T., S.Pe., Y.J.K., J.A.H. and N.A.E. provided technical assistance. A.C., S.N.O., F.P., H.R., G.M.M., A.L., E.S.F., Y.P. and X.S.L. contributed to critical experimental planning and resources. B.J.A. and S.A.A. wrote the first draft of the manuscript. All authors contributed to editing of subsequent manuscript drafts.

Acute myeloid leukaemia (AML) remains difficult to treat and requires new therapeutic approaches. Potent inhibitors of the chromatin-associated protein MENIN have recently entered human clinical trials, opening new therapeutic opportunities for some genetic subtypes of this disease. Using genome-scale functional genetic screens we identified *IKZF1*/IKAROS as an essential transcription factor in *MLL1*-rearranged (*MLL-r*) AML that maintains leukaemogenic gene expression while also repressing pathways for tumour suppression, immune regulation, and cellular differentiation. Furthermore, IKAROS displays an unexpected functional cooperativity and extensive chromatin co-occupancy with *MLL1*/MENIN and *MEIS1* and an extensive hematopoietic transcriptional complex involving *HOXA10*, *MEIS1* and IKAROS. This dependency could be therapeutically exploited by inducing IKAROS protein degradation with immunomodulatory imide drugs (IMiDs). Finally, we demonstrate that combined IKAROS degradation and MENIN inhibition effectively disrupts leukaemogenic transcriptional networks resulting in synergistic killing of leukaemia cells and providing a paradigm for improved drug-targeting of transcription, and an opportunity for rapid clinical translation.

KMT2A/MLL1 gene chromosomal translocations (*MLL-r*) define a distinct subset of Acute Myeloid Leukaemia (AML)^{1,2} characterized by well-defined pathologic features and a dismal prognosis. *MLL-r* AML serves as a paradigm for malignant disease that is driven by disordered gene expression³. Normal haematopoiesis is governed by a hierarchy of transcription factors (TFs) that mediate cell fate decisions while co-operating within densely interconnected co-regulatory circuits⁴. The *MLL*-fusion drives leukaemia through deregulation of these critical transcriptional networks, functioning within multi-component protein complexes containing key structural proteins and enzymes, including MENIN⁵, LEDGF⁶, DOT1L^{7,8}, and the super-elongation complex (SEC)⁹; each of which is important for *MLL*-fusion function. Acting within these complexes, the *MLL*-fusion drives the abnormal expression of numerous haematopoietic TFs such as *MEF2C*^{10,11}, *CDK6*¹², *HOXA9*¹³, *PBX3*¹⁴, and *MEIS1*¹⁵ which, in turn, mediate downstream transcriptional deregulation. These TFs interact with additional myeloid transcriptional regulatory proteins such as CEBP α ¹⁶, RUNX1¹⁷, *KMT2C/MLL3*¹⁸, *SPI1/PU.1*¹⁹ and JMJD1C²⁰, thereby impacting diverse cellular processes. Of these downstream oncogenic collaborators, *HOXA* cluster genes and *MEIS1*, which act together, are considered among the most important due to their ability to recapitulate much of the oncogenic function of the *MLL*-fusion protein^{13,21}. Considered broadly, the *MLL*-fusion acts within a complex network of transcriptional regulators that are essential for its leukaemogenicity, and elucidating strategies to shut down these pathways has been a major focus of therapeutic development for this disease. Furthermore, mechanisms that govern *MLL*-fusion driven gene expression are also critical for leukemia development in other subtypes of AML; of particular importance, high-level *HOX/MEIS* gene expression is observed in *NPM1*-mutant (*NPM1c*) AML²².

Deregulated transcription is an established hallmark of malignant disease²³ and a major target for the development of cancer therapeutics. *MLL-r* leukaemia serves as a model disease for this approach. Highly specific and potent small molecule inhibitors have been developed to target the MENIN-*MLL1* protein-protein interaction (VTP-50469²⁴, MI-503/463²⁵ and MI-3454²⁶), and also the enzymatic function of the

H3K79 methyltransferase, DOT1L (EPZ-5676^{27,28}), as a means to target the MLL-fusion-containing complex and downstream leukaemia-promoting transcription. These drugs exhibit potent antileukemic effects in pre-clinical models of both *MLL-r* and *NPM1c* leukaemia^{22,24,26,29}. Clinical-grade compounds related to VTP-50469 and MI-3454 have now entered Phase I/II clinical studies (*Syndax/SNDX-5613* and *Kura/KO-539*, respectively). The DOT1L inhibitor, EPZ-5676 (*Epizyme/Pinometostat*), has completed a Phase I/II clinical study³⁰, demonstrating on-target activity in humans but achieving only modest therapeutic effect, which highlights the need to understand resistance mechanisms and develop drug combinations to improve efficacy. Combination therapies are typically superior to monotherapy because they can abrogate resistance mechanisms, which is of particular importance for therapeutic targeting of transcriptional networks due to the presence of large multi-protein complexes containing cooperating TFs with functional redundancies that may be inefficiently targeted by a single drug alone³¹. With MENIN and DOT1L inhibitors entering clinical trials as single agent therapies, we sought to investigate how mechanisms of resistance may limit their clinical application and inform the rational development of more effective drug combinations. Remarkably, we identified IKAROS/*IKZF1* as an essential transcriptional regulator in *MLL-r* and *NPM1c* AML that can be immediately exploited using the immunomodulatory imide drugs (IMiDs); furthermore, we found that combined therapeutic targeting of IKAROS and MENIN leads to synergistic anti-proliferative effects and propose this as a novel therapeutic strategy for AML.

Results

IKZF1/IKAROS modulates dependency on MLL1-MENIN and DOT1L.

Genome-scale, CRISPR/Cas9-based functional genetic screening was used to characterize resistance mechanisms and synthetic lethal interactions for small molecule inhibitors of DOT1L or MENIN (EPZ-5676 and VTP-50469, respectively) using the human *MLL-r* AML cell line, MOLM13 (Fig. 1a). These drugs target the MLL-fusion complex³ (Fig. 1b). Cell proliferation was monitored during the screen (Extended Data Fig. 1a), showing strong inhibition. Comparison of the drug-treatment group to the vehicle-control on Day 14 (Supplementary Table 1) revealed selection for sgRNAs targeting transcriptional regulators (Extended Data Fig. 1b), and a strong overlap between the two drugs (Extended Data Fig. 1c). Leading edge analysis, focusing on resistance genes (Group 2) and synthetic lethal genes (Group 4), according to the MAGeCKFlute computational pipeline³², highlighted genes exerting a large effect size in both screens (Fig. 1e) and common mechanisms of resistance. A combined analysis of the two screens highlighted these common pathways (Fig. 1c) (Supplementary Table 1); *IKZF1/IKAROS* and *MTA2* were the two highest-scoring negatively-selected genes, which are notable as constituents of the nucleosome remodelling and histone deacetylase complex (NuRD)³³. Other high-ranking genes that were depleted or enriched included members of the SWI/SNF complex (*SMARCA4*, *SS18*), mTOR pathway (*TSC1*, *TSC2*, *PTEIN*), protein ubiquitination regulators (*UBE2A*, *BAP1*, *TBL1XR1*, *AMBRA1*, *UCHL5*, *RNF138*, *NOSIP*), regulators of histone methylation (*KDM5D/JARID1D*, *KDM5C/JARID1C*, *SETD1B*, *NSD1*, *KMT2C/MLL3*, *PRDM13*), transcription factors (*FOXA1*, *HOXA10*, *HOXB5*, *MEF2C*, *AHR*) and zinc-finger proteins (*ZNF410*, *ZNF460*, *ZNF182*, *ZNF548*, *ZNF596*). MAGeCKFlute was utilized to correct cell

cycle biases and classify hits into functional categories (Fig. 1d)³². This highlighted *IKZF1*, *MTA2*, and *HOXA10* as synthetic lethal gene targets, because they were disproportionately depleted in drug-treated cells, and identified these genes as therapeutic targets that may increase sensitivity to inhibition of MENIN and DOT1L. IKAROS is an established therapeutic target in lymphoproliferative disorders, but a role in *MLL-r* AML has not been previously reported. Notably, *IKZF1* exhibits high-level gene expression in human AML^{34,35} and is also detected as an AML dependency in the Broad DepMap ($p = 3.8 \times 10^{-12}$); across all cancer cell lines in the DepMap, there is a significant correlation of dependency between *MEN1* and *IKZF1* (Pearson 0.15, p -value 5.3×10^{-7}) and between *DOT1L* and *IKZF1* (Pearson 0.19, p -value 5.7×10^{-10})³⁵. We next evaluated the impact of genetic targeting of both *IKZF1* and *MTA2* using CRISPR/Cas9-based competition assays, using lentiviral vectors co-expressing a sgRNA and red fluorescence protein (RFP), in four different Cas9-expressing human *MLL-r* AML cell lines (MOLM13, MV4;11, OCI-AML2 and THP-1), revealing strong depletion of sgRNAs targeting *IKZF1* and *MTA2* (Fig. 1f and Extended Data Fig. 1d). Addition of VTP-50469 enhanced sgRNA depletion (Fig. 1f and Extended Data Fig. 2a), as predicted by the genetic screen. To generalize this finding to other leukaemia subtypes, two *NPM1c* cell lines (IMSM2 and OCI-AML3) and two non-*MLL*-rearranged leukaemias (U937 and HL60) were examined (Extended Data Fig. 1e); importantly, U937 and HL60 did not display IKAROS dependency and, notably, are also insensitive to MENIN-inhibition²⁴, highlighting a context-dependent role for IKAROS. In contrast, both *NPM1c* cell lines exhibited strong IKAROS dependency in accordance with their overlapping gene expression profile with *MLL-r* AML³⁶ and dependency on DOT1L/MENIN²², suggesting that IKAROS and MENIN may be co-dependencies. CRISPR/Cas9-mediated depletion of IKAROS and MTA2 protein was confirmed by Western blot (Extended Data Fig. 2b,c). Cell proliferation was measured following *IKZF1* knock-out, with and without MENIN or DOT1L inhibition, revealing a modest reduction in cell proliferation that was enhanced when combined with either the MENIN or DOT1L inhibitor (Fig. 1g); *IKZF1* knockout in combination with the MENIN inhibition resulted in the strongest overall anti-proliferative effect, shifting of the IC50 of MENIN inhibition (Fig. 1j, Extended Data Fig. 2f), and substantially increasing the amount of apoptosis induced with MENIN inhibition (Extended Data Fig. 2g). Remarkably, loss of either *IKZF1* or *MTA2* led to cellular differentiation, induction of apoptosis (Extended Data Fig. 2d), and morphologic changes consistent with monocytic differentiation (Fig. 1h), indicating that *IKZF1* and the NuRD complex have a fundamentally important role in leukaemia maintenance. Additionally, *IKZF1* loss impaired colony formation in colony forming assays. (Fig. 1i, Extended Data Fig. 2e) and in a MOLM13 xenograft experiment, *IKZF1* knockout enhanced MENIN inhibition in terms of reducing burden of disease and increasing differentiation markers *in vivo* (Fig. 1k,l), further implicating *IKZF1* as essential to *MLL-r* leukemia maintenance.

IMiDs efficiently drive IKAROS protein degradation in AML.

We next sought to leverage this finding by targeting IKAROS protein in AML using IMiDs. Lenalidomide, and related thalidomide-analogues, promote Cereblon (CRBN)-mediated degradation of the *neo*-substrates IKAROS, AIOLOS^{37,38}, Casein Kinase 1 α (CK1 α)³⁹ and others. Thalidomide (THAL), and newer generation IMiDs, lenalidomide (LEN),

pomalidomide (POM) and iberdomide (CC220), display differing *neo*-substrate profiles and potency of IKAROS protein degradation⁴⁰. Detailed evaluation of these drugs in *MLL-r* AML has not been previously reported. Thus, we evaluated all 4 drugs for potency of IKAROS degradation in three *MLL-r* human AML cell lines (Fig. 2a and Extended Data Fig. 3a,b); increasing potency of IKAROS degradation was observed for THAL, LEN, POM and CC220, respectively. Each IMiD impaired cell proliferation in a manner correlating with the depth of IKAROS degradation (Fig. 2b) and, notably, a defect in proliferation was not observed until 6–9 days. The therapeutic dose-response relationship was strongly correlated with the degree of IKAROS degradation (CC220>>POM>LEN>>THAL) (Fig. 2c,d). In accordance with genetic deletion, IMiD treatment also impaired proliferation of the *NPM1c* AML cell lines, IMSM2 and OCI-AML3 (Extended Data Fig. 3c). A detailed *neo*-substrate profile for each drug in all 3 *MLL-r* cell lines tested (MV4;11, MOLM13, OCI-AML2) was determined using multiplexed mass spectrometry (MS)-based global proteomics. This confirmed IKAROS as the primary *neo*-substrate (Fig. 2e and Extended Data Fig. 3d; Supplementary Table 2) without obvious novel *neo*-substrate degradation detected; notably, *ZFP91* and *ZNF692* are not detected as AML dependencies in the *Depmap* (data not shown). CK1 α peptides were not efficiently detected by MS but confirmed by Western blot analysis to only be a substrate of LEN (Extended Data Fig. 3a,b); CC220 elicited the most potent inhibitory effect on cell growth while exhibiting profound IKAROS degradation and minimal effect on CK1 α , consistent with IKAROS being the primary substrate mediating these effects. Further, overexpression of a non-degradable IKAROS mutant with a single amino acid substitution rendering it not capable of being degraded (Q146H)³⁸, rescued the antiproliferative effects of IMiDs (Fig. 2f,g,h). Altogether, these data support IMiDs as a potential novel therapeutic approach for *MLL-r* AML through their ability to degrade the IKAROS protein.

IKAROS is a core transcriptional regulator in *MLL-r* AML.

We next determined the transcriptional changes following IKAROS degradation in *MLL-r* AML using RNA-sequencing (RNA-seq) (Fig. 3a; Supplementary Table 3). LEN and CC220 displayed highly correlated gene expression changes (Extended Data Fig. 4a). Gene set enrichment analysis (GSEA) highlighted gene expression changes related to *HOXA9* (Fig. 3b), stem cell biology, myeloid differentiation, MTOR pathway, inflammatory/immune signalling and cell death regulators (Extended Data Fig. 4c,d). Remarkably, after 6 days of LEN treatment, the critical pro-survival gene, *BCL2*, was the most significantly down-regulated gene in the MV4;11 cell line (Extended Data Fig. 4b; Supplementary Table 3). IKAROS degradation resulted in induction of gene expression associated with myelomonocytic differentiation and loss of stem cell-associated genes (Fig. 3b), demonstrating therapeutic response at the level of transcription and indicating that IKAROS is required to sustain the differentiation block. IMiD treatment perturbed the expression of *HOXA9* target genes without impacting the expression of the *HOXA9* gene itself, or other canonical MLL-fusion target genes (Fig. 3c), implicating a functional interaction between IKAROS and *HOXA/MEIS1*. The *HOXA/MEIS1* transcriptional program is considered critical for the oncogenicity of the MLL-fusion protein^{13,21} and is a shared feature with *NPM1c* AML³⁶. More broadly, IKAROS loss impacted non-canonical MLL-fusion target genes, including *FLT3* and *BCL2* (Extended Data Fig. 4e)^{8,41}. Prominently, IMiD

treatment strongly activated pathways involving the immune response (*SOX4*, *SOCS2*, TREM signalling, the TNF pathway, IL6/STAT-signalling, HLA gene expression) (Extended Data Fig. 4f), also suggesting an important role for IKAROS in immune-regulation in AML.

We next defined genome-wide chromatin occupancy for IKAROS, using a combination of chromatin immunoprecipitation followed by next-generation DNA-sequencing (ChIP-seq) and the Cleavage Under Target and Release Using Nuclease (CUT&RUN)⁴²⁻⁴⁴. To delineate IKAROS occupancy at functional regulatory regions, we defined a genome-wide map of enhancers and enhancer-promoter connections using the activity-by-contact (ABC) model⁴⁵. ChIP-seq revealed widespread IKAROS-binding in MOLM13 (21,816 peaks showing >5-fold enrichment (FE) over background) and MV4;11 (50,897 peaks at >5FE) with frequent occupancy in proximity to transcriptional start sites (TSS) (<1kb from the TSS) and at enhancers (Fig. 3d) (also see Fig. 6b,c and Extended Data 8b,c; Supplementary Table 4). In MOLM13, 8079 genes exhibited an IKAROS peak in proximity to the TSS, including many MLL-fusion- and HOXA9-regulated genes (Fig. 3e). A context-dependent role for IKAROS was observed with substantial cell line-specific gene expression changes (Extended Data Fig. 4g). Globally, IKAROS-bound TSSes were strongly predictive of gene expression changes (Extended Data Fig. 4h) with a modest predominance of activated gene expression. Extensive IKAROS occupancy was also noted at enhancers (including those for *MYC*, *BCL2*, *FLT3*, *MYB*, and *TNF*) and this also correlated with gene expression changes using enhancer-gene connection predictions by the ABC model. Notably, many genes exhibited IKAROS peaks at their TSS as well as a connecting enhancer (Fig. 6b,c and Extended Data 8b,c) and approximately 30% of all genes deregulated following IMiD treatment were found to have an associated IKAROS-bound enhancer (Extended Data Fig. 4i). We next used CUT&RUN to define the repertoire of TF binding motifs present at IKAROS-bound sites. Discriminative Regular Expression Motif Elicitation (DREME) detected two motifs with homology to reported *IKZF1* motifs (Extended Data Fig. 5a) among the highest-ranking motifs in both cell lines (Fig. 3f); CTCF and IgG were used as positive and negative controls, respectively (Extended Data Fig. 5b,c). IKAROS peaks were bound at motifs for critical myeloid TFs (Fig. 3f and Extended Data Fig. 5d) including those for the *ETS*-family (*FLI1/SPI1/Pu.1*), *RUNX1/2/3/CBFB*, *SPI*, *CEBPα/NF-Y*, and *JUN:FOS*. Notably, all of these TFs play an important role in transcriptional deregulation by the MLL-fusion, placing IKAROS within this critical transcriptional network. Overall, these findings position IKAROS as a core transcriptional regulator in *MLL-r* AML.

Co-targeting MENIN and IKAROS drives synergistic cell death.

We next evaluated combined IKAROS degradation using IMiDs and MENIN inhibition using VTP-50469. Combined treatment resulted in more potent antiproliferative effects compared to VTP-50469 alone (Fig. 4a). VTP-50469 drives a cellular response typified by cell cycle arrest and differentiation²⁴; however, when used in combination with IMiDs, early loss of cell number was observed due to marked, early induction of apoptosis (Fig. 4b and Extended Data Fig. 6a), representing a potent switch from VTP-50469-induced differentiation to apoptotic cell death. IMiD treatment alone was sufficient to produce immunophenotypic evidence of differentiation and cell cycle arrest, and this was enhanced with combination treatment (Extended Data Fig. 6b,c). The IMiD-VTP-50469 combination

displayed synergy, with the response correlative to the potency of IKAROS degradation (CC220>LEN) (Fig. 4c and Extended Data Fig. 6d,e). The IMiD effect was rescued by overexpression of a non-degradable IKAROS mutant (Extended Data Fig. 6f,g). To assess for toxicity to normal hematopoietic cells, we treated non-transformed CD34+ cells and *MLL-AF9* transformed CD34+ cells, demonstrating a potential therapeutic window (Fig. 4d). Given the profound apoptotic response, we used MS to exclude the possibility that concomitant VTP-50469 treatment may alter the IMiD *neo*-substrate profile (Extended Data Fig. 6h; Supplementary Table 2). To characterize the mechanism of enhanced apoptosis, we evaluated apoptotic priming using BH3-profiling⁴⁶. At baseline, the MV4;11 and MOLM13 cell lines were primarily dependent on BCL-2 for survival, based on mitochondrial sensitivity to BCL-2 selective ABT-199 (Day 1; Fig. 4e and Extended Data Fig. 6i). With combination treatment, the cells became globally primed for apoptosis (increasing BIM sensitivity on Day 3), which progressed to a state of initiated apoptosis (no peptide) by Day 4. On day 3, cells showed a dramatic increase in sensitivity to targeting of MCL-1 and BCL-XL (MS1 for MCL-1; HRK and A113 for BCL-XL), which is in keeping with loss of *BCL2*-expression following IKAROS degradation (Extended Data Fig. 6j) while MCL1 and BCL-XL protein levels remain unchanged. Remarkably, this combination converts two small molecules that primarily induce differentiation into potent inducers of cell death.

MENIN and IKAROS support leukaemia-promoting transcription.

We next evaluated the impact of IKAROS degradation on the transcriptional response to MENIN inhibition (Fig. 4f). Surprisingly, IMiD and VTP-50469 treatments produced strongly overlapping transcriptional changes (Fig. 4f,g) and a large number of genes differentially expressed only with the combination. For MOLM13, 42% of all differentially expressed genes by CC220 (>2 FC) were shared with VTP-50469 and 1095 genes (54.6% of the combination drug response) were unique to the drug combination (Extended Data Fig. 7a). Therefore, numerous genes are commonly regulated by IKAROS and MENIN (Extended Data Fig. 7b,c) and many are only perturbed under combination treatment. GSEA identified *HOXA9* and *MYC* among pathways accentuated by the combination (Fig. 4h,i) as compared to VTP-50469 monotherapy. This finding demonstrates that although VTP-50469 drives rapid downregulation of *MEIS1* gene expression, combined IKAROS targeting results in more profound disruption of the downstream HOX/MEIS-regulated network; importantly, combined IKAROS-targeting did not impact the VTP-50469 effect on *MEIS1*, *HOXA9* or *HOXA10* gene expression. Combination treatment led to further down-regulation of *MYC* and *BCL2* gene expression (Fig. 4j). Reduction in BCL2, MYC and GATA2 protein levels was confirmed by Western blot (Fig. 4k,l), and there was loss of cell surface expression of FLT3 protein (Extended Data Fig. 7d). Notably, *MYC*, *BCL2* and *FLT3* were all identified as strong dependencies in MOLM13 (Extended Data Fig. 7e). MENIN inhibition significantly altered expression of genes also deregulated following IKAROS degradation (Fig. 5a) prompting examination of IKAROS protein levels under VTP-50469 treatment. VTP-50469 caused substantial loss of IKAROS protein over 72 h (Fig. 5b) that was additive with the IMiD-VTP-50469 combination (Fig. 5c) and associated with compensatory increase in *IKZF1* gene expression (Extended Data Fig. 7f). VTP-50469-induced loss of IKAROS protein was partially rescued using the proteasome inhibitor, bortezomib (BTZ) (Extended Data Fig. 7g), in keeping with IKAROS loss via proteasomal degradation. Furthermore,

MENIN inhibitor treatment led to loss of IKAROS binding proximal to TSSes (Extended Data Fig. 7h) and loss of the IKAROS footprint over the *IKZF1* motif (Fig. 5d), directly linking MENIN with the regulation of IKAROS protein stability.

IKAROS, MENIN/MLL1 and MEIS1/HOXA chromatin co-occupancy.

We next profiled the genome-wide chromatin binding of IKAROS in relation to the key regulators of these transcriptional programs: MEIS1, MLL1, and MENIN. Significant overlap was observed between IKAROS and each of the other factors (Extended Data Fig. 8a), with a high level of co-occupancy between IKAROS and MENIN proximal to TSSes and co-occupancy of IKAROS and MEIS1 at enhancers (Fig. 6a,b,c). MENIN-bound TSSes showed co-occupancy with IKAROS at 62.0% and 85.2%, for MOLM13 and MV4;11, respectively, while IKAROS-bound enhancers showed co-occupancy with MEIS1 at 81.4% and 62.8%, for MOLM13 and MV4;11, respectively. IKAROS co-occupancy peaks with MEIS1 were detected at enhancers with predicted connections to genes exhibiting IKAROS peaks proximal to the TSS (Fig. 6c and Extended Data Fig. 8b,c). Thus, IKAROS is extensively intertwined on the chromatin with MENIN, MLL1 and MEIS1. To investigate how IKAROS may be engaged in protein complexes at these locations, we examined the IKAROS, MEIS1 and HOXA10 proximal interactome using global proteomic proximity-based in-cell labelling (BioID)⁴⁷. BioID utilizes an engineered promiscuous biotin ligase, BirA* (~10 nm labelling radius), fused to a protein of interest enabling biotinylation of direct and proximal interacting proteins; IKAROS, MEIS1, HOXA10 and, as a control, ZNF692 were cloned with BirA* to produce fusion proteins that were constitutively expressed in MV4;11 and MOLM13 (Extended Data Fig. 8d,e). ZNF692 is a zinc finger containing transcription factor used as a control because it is not a dependency in *MLL-r* leukaemia and was considered an inert chromatin binding control. Stable BioID cell lines were grown in the presence of biotin for 24 hours prior to nuclear isolation, lysis, streptavidin capture of biotinylated proteins, on-bead tryptic digestion and LC-MS/MS analysis. Proteins were first ranked by peptide spectral matches (PSM) (Fig. 6d and Supplementary Table 7); IKAROS BioID strongly detected CHD4, CHD3, MTA2, MTA1, GATAD2A (p66 α) and GATAD2B (p66 β), confirming its association with the NuRD complex. IKAROS BioID analysis also detected interactions with *KMT2B/MLL2*, DOT1L and *KMT2A/MLL1*, suggesting proximity between IKAROS and MLL1-containing protein complexes. IKAROS BioID enriched for proteins associated with active enhancers (P300, CREBBP, *KMT2C/MLL3*, *KMT2D/MLL4*, NCOA6, and *KDM6A/UTX*) and myeloid TFs (HOXA10, CEBPA, RUNX1, RUNX2, ETV6 and PBX2). Complementary to these findings, HOXA10 and MEIS1 BioID both enriched for IKAROS and components of the NuRD complex. Protein abundances were also determined using label free quantitation (LFQ) and expressed relative to the control construct, ZNF692 (Fig. 6e, Extended Data Fig. 8d and Supplementary Table 8), with findings consistent with the PSM analysis. Striking overlap among enriched proteins by the IKAROS, MEIS1 and HOXA10 BioID systems was observed (Fig. 6f and Extended Data Fig. 8f,g), which included numerous TFs (IKAROS, MEF2A/C/D, ETV6, RUNX1/2/3, TLE1/3, ZEB2, GFI1, FLI1, MYB, and HOXA10). The BioID data confirms, at the level of protein-protein proximity, that IKAROS is physically intertwined within the core transcriptional circuitry of *MLL-r* leukaemia. MENIN was poorly detected by LC-MS/MS so we further explored the possibility that

IKAROS may be a constituent of an isolatable MENIN-containing chromatin complex using co-immunoprecipitation (Co-IP). Co-IPs using antibodies specific to 1) MENIN or MLL1, and 2) IKAROS, resulted in enrichment of IKAROS and MENIN, respectively (Fig. 6g,h and Extended data Fig. 9b,c,d,e), suggesting the presence of shared protein complex(es); in contrast, co-immunoprecipitation using IKAROS as bait did not enrich for MEIS1 and HOXA9 under these experimental conditions. Finally, we found that inhibition of the MENIN-MLL1 protein-protein interaction by VTP-50469 disrupted MENIN-IKAROS co-immunoprecipitation (Extended Data Fig. 9f). We propose that dual targeting of this putative protein complex containing MENIN and IKAROS contributes to the observed drug synergy.

Combined therapeutic effect of VTP-50469 and LEN *in vivo*.

LEN monotherapy and the VTP-50469 combination were then evaluated for *in vivo* efficacy. We evaluated LEN because it is supported by clinical experience, good safety profile, and multiple FDA approvals⁴⁸, providing opportunity for rapid clinical translation. LEN exhibits high oral bioavailability and has been used in mouse models⁴⁹; in contrast, CC220, although a more potent IKAROS degrader, exhibits poor oral bioavailability and has more limited use *in vivo*. We utilized three *MLL-r* and one *NPM1c* AML patient-derived xenograft (PDX) models (Fig. 7a). Human PDX cells were transplanted into non-conditioned immunodeficient recipient mice and, following engraftment, treatment was commenced with vehicle-control, LEN 50 mg/kg daily PO, continuous VTP-50469 in rodent special diet or the drug combination. Combination treatment led to more rapid clearance of leukaemia cells from peripheral blood compared with VTP-50469 alone ($p=0.024$) (Fig. 7b) and induced strong myelomonocytic differentiation (Fig. Extended Data Fig. 10b). After 7–21 days of treatment, according to VTP-50469 sensitivity of each PDX model, mice were sacrificed for analysis. LEN monotherapy reduced bone marrow disease burden (Fig. 7c), demonstrating *in vivo* efficacy for IMiD monotherapy in *MLL-r* AML. Furthermore, mice receiving combination treatment displayed a further reduction in bone marrow infiltration compared to either monotherapy (Fig. 7c and Extended Data Fig. 10a) with morphologic evidence of differentiation. LEN and combination-treated mice exhibited evidence of apoptosis induction in accordance with improved clearance of leukaemia (Extended Data Fig. 10c,d). We used RNA-seq to evaluate gene expression changes for each drug *in vivo*. This confirmed a strong *in vivo* effect of LEN in altering transcription (Fig. 7d; Supplementary Table 3). LEN elicited expression of differentiation-associated genes (Fig. 7d) and enhanced the VTP-50469 effect when used in combination (Extended Data Fig. 10e,f). An enhanced effect on the HOXA9 transcriptional program was observed *in vivo* (Extended data Fig. 10g) and LEN resulted in downregulation of MLL-fusion target genes (Extended data Fig. 10h). Ingenuity upstream regulator analysis using IPA showed upregulation of pathways associated with myeloid differentiation, immune activation/inflammation (*LPS*, *TNF*, *IL1*, *INFG*) and tumour suppressor pathways (*TP53*) (Extended Data Fig. 10i). Finally, we evaluated whether LEN monotherapy and the VTP-50469 combination improves survival. LEN monotherapy at 50 mg/kg once daily resulted in a modest survival advantage (Fig. 7e,f,g,h), which could be improved by increasing the dose to 50 mg/kg twice daily (Fig. 7f); combination treatment extended survival of the mice compared to VTP-50469 monotherapy in all three *MLL-r* models. In the *NPM1c* PDX, survival was extended by LEN

monotherapy, indicating efficacy for the IMiDs in this distinct AML sub-type, but the drug combination did not significantly extend survival compared to VTP-50469 monotherapy although it resulted in more rapid clearance of leukemia cells from the peripheral blood (Extended Data Fig. 10j). These studies demonstrate *in vivo* efficacy using a series of human PDX AML models, supporting this approach as a novel treatment strategy for patients with *MLL-r* AML.

Discussion

Genome-scale functional genetic screening in *MLL-r* AML identified mechanisms of drug resistance to clinically relevant DOT1L (EPZ-5676) and MENIN (VTP-50469) inhibitors, and guided the design of a highly effective combination drug treatment using IMiDs. EPZ-5676 and VTP-50469 therapeutically target *MLL-r*-driven transcriptional dependencies. We identified pathways toward drug resistance involving transcriptional regulators and chromatin remodelling complexes (e.g., NuRD and SWI/SNF), suggesting that cells can undergo transcriptional alterations to escape the effect of these drugs. Complementary to this finding, we found that concomitant targeting of transcriptional regulators that support leukaemogenic transcription, such as *IKZF1*/IKAROS, enhance the therapeutic effect of these drugs.

We found a diverse role for IKAROS in supporting leukaemia-promoting gene expression, including HOXA/MEIS1-driven gene expression, and repressing pathways for tumour suppression, immune signalling and differentiation. IKAROS function during haematopoiesis has been extensively studied in the lymphoid lineage due to its role as a tumour suppressor in acute lymphoblastic leukaemia and therapeutic target in multiple myeloma; however, less is known about its role in myeloid neoplasia. The *IKZF1* gene is expressed and tightly regulated throughout myeloid maturation, and loss of *IKZF1*/IKAROS during normal haematopoiesis impairs myeloid maturation⁵⁰. Patients with germline dominant negative *IKZF1* gene mutations exhibit multi-lineage haematopoietic defects including abnormal myeloid maturation⁵¹. Furthermore, IKAROS is a critical regulator of haematopoietic stem/progenitor cell function, implying a potential role AML stem cell function⁵². Loss of IKAROS in a cell line model of del(5q) myelodysplastic syndrome results in megakaryocytic differentiation⁵³, reflecting features that we observed in *MLL-r* AML. In *MLL-r* AML, we found that IKAROS regulates diverse, essential transcriptional processes while displaying extensive chromatin co-occupancy with key regulators of the *MLL-r* transcriptional program: MLL1, MENIN and MEIS1. This is in keeping with known functions of IKAROS: IKAROS can mediate transcriptional repression and activation via recruitment of the NuRD complex⁵⁴, it can support active transcription through recruitment of the SWI/SNF complex⁵⁴ and SEC⁵⁵, and can also act as a pioneer TF with enhancer remodelling activity⁵⁶. Thus, we identify IKAROS is a central component of a TF-driven circuitry in *MLL-r* AML, and likely other AML subtypes that are dependent on HOX/MEIS1 driven gene expression like *NPM1c* AML.

IKAROS displays extensive chromatin co-occupancy with MENIN, MLL1, and MEIS1, with a pattern of overlap suggesting a role for co-occupancy of IKAROS and MEIS1 at enhancers and a distinct co-occupancy involving MENIN, MLL1 and IKAROS proximal

to the TSS. Of particular note, proximity labelling experiments using BioID revealed that IKAROS, MEIS1 and HOXA10 share a similar proximal protein environment populated by important transcriptional regulatory protein complexes such as NuRD and MLL3/4 COMPASS as well as transcription factors well known for their role in hematopoietic development and leukemia. This nominates IKAROS as a critical regulator of myeloid leukemia associated gene expression. Furthermore, these data define the proximal protein network that comprises the HOXA10/MEIS1 regulatory complex, which is central to hematopoietic development and multiple AML subtypes. Notably, MEIS1/HOXA9 has been reported to play a key role in enhancer regulation¹⁸ and MENIN is thought to primarily act proximal to the TSS⁵⁷, whereas IKAROS has diverse described functions at both the TSS and enhancer⁵⁴ supporting a role for IKAROS at both of these locations in *MLL-r* AML. Importantly, chromatin co-occupancy at the TSS by IKAROS and MENIN raises the possibility that IKAROS may participate in the MLL-fusion protein complex. In support of this possibility, IKAROS and other components of the NuRD complex have been previously reported to co-immunoprecipitate with seven different MLL-fusion proteins⁵⁸. Interestingly, as a sequence-specific DNA-binding protein, IKAROS could potentially play a role in directing the genomic localization of the MLL-fusion and other components of its transcriptional network. It is also important to note that outside of its well-defined protein-protein interaction with *KMT2A/MLL1*⁵⁹ and the MLL1-fusion protein⁵, MENIN is reported to interact with a number of TFs including c-MYC⁶⁰ and JUND^{61,62}, which may be akin to our observations for IKAROS. We also found post-translational loss of IKAROS protein following treatment with the MENIN inhibitor, similar to what has been described for MENIN^{24,63} and partially attributed to its eviction from stabilizing chromatin-bound complexes; we hypothesize that IKAROS may be similarly stabilized within such chromatin-bound complexes involving MENIN/MLL1 that then become destabilized following MENIN inhibitor treatment. Indeed, we find that IKAROS exhibits a physical interaction with both MENIN and MLL1 (albeit this may be direct or through interaction with a larger multi-protein complex) using a series of targeted Co-IPs.

From the perspective of clinical translation, these findings support a novel therapeutic approach for the treatment of *MLL-r* AML, using drugs that target IKAROS for degradation in combination with small molecule inhibitors of MENIN and DOT1L. IMiDs have already been evaluated in numerous clinical trials for AML⁶⁴ with encouraging but variable evidence for efficacy, however these trials have not evaluated specific leukaemia sub-types. The rationale for using these drugs in the setting of AML has been attributed to targeting CK1 α ⁶⁵, immune modulation⁶⁶ and activation of calpain-dependent⁶⁷ apoptosis. In addition to these important features of the IMiD mode of action, we present data that therapeutic targeting of IKAROS is a critical determinant of the drug's efficacy in AML, supporting the optimization of IMiD-induced IKAROS degradation as a goal for improved AML therapeutics. Having defined overlapping functions of MENIN and IKAROS in *MLL-r* AML, we show that combined therapeutic targeting of these two AML dependencies leads to profound anti-leukemic effects both *in vitro* and *in vivo*, supporting this as a novel therapeutic approach and highlighting an essential functional interaction between MENIN and IKAROS in leukemic transcriptional regulation. This serves as an example of dual therapeutic targeting of a robust transcriptional network, and putative chromatin-bound

protein complex, that more effectively shuts down its oncogenic function compared to either drug alone. Furthermore, combining MENIN inhibition and IKAROS degradation converts two small molecules that primarily induce AML differentiation into a combination that potently induces apoptosis, an effect that is predicted to provide therapeutic benefit.

Online Methods

Animals and patient-derived cells

Animal experiments were approved by Dana-Farber Cancer Institute's (DFCI) Institutional Animal Care and Use Committee (IACUC) (DFCI protocol number: 16-021; Principal Investigator: Scott Armstrong). Patient-derived xenograft (PDX) models were provided by the Center for Pediatric Cancer Therapeutics (CPCT) at DFCI. CPCT-0007 is a newly generated model: primary human leukemic cells obtained from the Pediatric LEAP Consortium were injected intravenously (IV) to sub-lethally irradiated (200Gy, 4 hrs prior to injection) 6–8 week old NSG-S mice (genotype: NOD.Cg-Prkdc^{scid} Il2rg^{tm1Wjl} Tg(CMV-IL3,CSF2,KITLG)1Eav/MloySzJ) (Jackson Laboratory; Stock #013062). When animals developed signs of leukaemia, bone marrow and spleen were harvested, and cells were frozen for banking purposes. After secondary transplantation, samples were analysed using a targeted next-generation sequencing panel (Rapid Heme Panel, Brigham and Women's Hospital)⁶⁸. The source patient (0.75 y male) had refractory *MLL*-r AML. CBAM-68552^{24,69} and DFAM-16835 were previously described²⁹, and CBSK-17D was a kind gift from Dr. Ross Levine, Memorial Sloan Kettering Cancer Center. Laboratory mice are housed in solid-bottom, polysulfone 75 sq. in. microisolator cages. The cages are used in conjunction with the Optimice® rack systems with integrated automatic watering. Temperature and humidity in the rodent facilities are controlled at 72 +/- 2°F and a target range of 35–55% relative humidity. A standard photoperiod of 12 hours light/12 hours dark is controlled by an automated system.

Cell lines

Cell lines were acquired from American Type Culture Collection (ATCC) or the Deutsche Sammlung von Mikroorganismen und Zellkulturen (DSMZ), as indicated: HEK293T cells (ATCC #CRL-3216), MOLM13 (DSMZ Cat#ACC554), MV4;11 (ATCC Cat#CRL-9591), OCI-AML2 (DSMZ Cat#ACC-99), THP-1 (ATCC Cat#TIB-202), OCI-AML3 (DSMZ Cat#ACC-582), U937 (ATCC Cat#CRL-1593.2), and HL60 (ATCC Cat#CCL-240). The IMS-M2 cell line (*NPM1c*) was a kind gift from Dr. Daniel Tenen, Harvard Medical School, with original source as previously described⁷⁰. Identification cell lines was independently confirmed by cytogenetics profiling. Routine mycoplasma testing was negative. Cells were cultured in RPMI 1640 (Gibco Cat #11875-093) supplemented with 10% foetal bovine serum, 100U/mL penicillin (Gibco), 100 µg/mL streptomycin (Gibco), and L-glutamine 2 mM at 37°C and 5% CO₂.

Genome-scale functional genetic screen

Functional genetic screening was carried out as previously described⁷¹ using paired whole genome libraries (denoted H1 and H2) (Addgene Cat#1000000132). Each library contains approximately 90,000 sgRNAs with 5 sgRNAs per gene and a panel of *AAVS1* negative-

control sgRNAs. The H1 and H2 libraries, combined, target over 18,000 genes with a total of 185,634 sgRNAs. The sgRNA vector combines both Cas9 and sgRNA expression along with puromycin resistance cassette in a single construct. The H1 and H2 libraries were prepared by electroporation (10 μ F, 600 Ohms, 1800V) of *E. coli high efficiency bacteria* (Lucigen) and culture on agar plates overnight prior to DNA purification using maxi-prep DNA purification columns (Invitrogen Cat #K210017). Prepared libraries were sequenced prior to performing the screen, showing a Gini index <0.1, zero sgRNA count <0.5% and sgRNA representation of the parental library >99.5%. Virus production was carried out on 10 cm plates using HEK293T cells with 10 μ g library plasmid per 10 cm plate along with packaging plasmids psPAX2 (Addgene#12260) (7.5 μ g) and pMD2.G (Addgene#12259) (3 μ g). X-tremeGENE 9 DNA transfection reagent (Sigma-Aldrich) was used to deliver DNA in HEK293T cells, in OPTI-MEM media (Gibco#31985062). Viral supernatant was collected at 24 and 48 h, and pooled. Viral supernatant was titrated to produce a multiplicity of infection (MOI) of approximately 0.2. For each experimental replicate, 50×10^6 cells were infected with an MOI of 0.2 resulting in $\sim 10 \times 10^6$ transduced cells, providing for 100x coverage of the sgRNA library. Infections were carried out as a 2 h co-incubation with viral supernatant followed by 2 h centrifugation at 800g, 37°C. After 48 h recovery time from infection, cells were placed in puromycin (1 μ g/mL) for 72 h to enrich for sgRNA-transduced cells. Cells were then collected and placed in fresh medium to recover for a further 48 hr prior to commencing the screen. Library coverage of 300X (30×10^6 cells) was maintained throughout the experiment. Cell pellets were obtained at Day 0 and Day 14 containing 30×10^6 cells. Cells were washed in phosphate-buffered saline (PBS) and lysed in 8 mL lysis buffer (NaCl 300 mM, SDS 0.2%, EDTA 1mM, Tris-HCL pH 8.0 10 mM). Samples were then incubated with RNAase A (100 μ g/mL) for 1 h at 65°C and then overnight with proteinase K (100 μ g/mL) at 55°C on constant rotation. Genomic DNA was then purified by phenol:chloroform extraction. Amplicon sequencing libraries were then produced using 200 μ g of genomic DNA from each experimental replicate, as follows: a first-round PCR reaction, in 32 separate 100 μ L reactions, using Q5 High-Fidelity DNA Polymerase (NEB) to amplify the region of the sgRNA between U6 and EF-1 α using primers: forward: AATGGACTATCATATGCTTACCGTAACTTGAAAGTATTTTCG and reverse: TCTACTATTCTTTCCCCTGCACTGTACCTGTGGGCGATGTGCGCTCTG; the product was pooled from the primary PCR reaction. a second PCR was carried out to incorporate Illumina adaptors and a 6bp barcode for identification of samples (Supplementary Table 5). A third PCR reaction was carried out to enrich for full-length amplicon using primers: forward AATGATACGGCGACCACCGAGATC and reverse CAAGCAGAAGACGGCATAACGAGAT. Final amplicon libraries were purified by gel electrophoresis and extraction of the library followed by gel purification using the QiaQuick Gel Extraction Kit (Qiagen Cat#28704). Sequencing carried out by Novogene Incorporated, Inc., and analysed using the MAGECK and MAGECKFlute computational pipeline^{32,72}. FASTQ files were converted to read count tables using the MAGECK *count* command. Each genetic screen was carried out in n=2 replicates for each of the H1 and H2 libraries (total n=4 for each drug and control condition). H1 and H2 libraries were combined into a single analysis using the MAGECK maximum likelihood estimation (MLE) function using read-normalized count tables and *AAVSI* normalization. MLE calculations were then analysed using the MAGECKFlute package in *R Studio* to apply corrections for cell cycle

bias and categorize genetic hits as pathway (group 1), resistance (group 2) and synthetic lethal (group 4). For the combined EPZ-5676/VTP-50469 analysis, each set of screens were treated as experimental replicates and analysed using the MAGeCK MLE function followed by MAGeCKFLUTE.

Drug treatment studies: *in vivo*

For PDX experiments, 1×10^6 human cells were injected into the tail vein of non-irradiated NOG-F mice (NOD.Cg-*Prkdc^{scid} Il2rg^{tm1.Sug}/JicTac*) (Taconic BioSciences, USA). For the cell line xenograft experiment, MOLM13 Cas9-expressing cell lines with sgRNA against *Luciferase* (non-targeting, NT) and two sgRNAs against *IKZF1* were used. All transplanted mice were female, aged between 8–10 weeks on delivery to the facility, and injected 1–2 weeks thereafter. Drug treatment began after engraftment was confirmed by flow cytometric detection of human CD45 expressing cells in the peripheral blood. VTP-50469-containing chow (0.1% and 0.03%, as indicated) was provided by *Syndax* pharmaceuticals. Lenalidomide (MedChem Express) was reconstituted in 0.5% carboxymethylcellulose (Sigma C4888), 0.25% Tween 80 (Sigma P1754), in water, and sonicated until forming a homogenous suspension immediately prior to dosing by oral gavage. Peripheral blood leukaemia burden was monitored by blood sampling. Blood samples were red cell lysed using Pharm Lyse (BD Cat#555899) prior to staining with phycoerythrin (PE)-conjugated anti-human CD45 antibody (BioLegend Cat#304058) 5 uL antibody per 100 uL solution, BV421-conjugated anti-CD11b (Biolegend)) 5 uL antibody per 100 uL solution and APC-conjugated anti-CD14 (BioLegend)) 5 uL antibody per 100 uL solution, as indicated. Samples were then analysed on an LSR Fortessa flow cytometer (Becton Dickinson). For survival experiments, mice were sacrificed when showing signs of illness. We adhered to DFCI standard operating procedure for humane experimental endpoints, which includes tumours measuring 2 cm, ulceration or infection of the tumor site, tumours which compromise mobility, tumours that have become necrotic, weight loss exceeding 15% of the animal's body weight, interference with the animal's ability to eat, drink, urinate or defecate, and anorexia. Leukaemia burden was assessed by measuring human CD45 positive cells by flow cytometry or by immunohistochemistry (ServiceBio, Inc., Boston, MA).

Drug treatment studies: *in vitro*

All drugs were diluted from stock solutions into full tissue culture medium (RPMI+10% FBS). Bortezomib (Thermo Fisher) was reconstituted in DMSO at 10 mM stock solution and used at a final working concentration of 50 nM. QVD-OPh (Abcam) 10 mM stock solution was diluted to a final working concentration of 10 μ M. All IMiD drugs were obtained from MedChemExpress: Thalidomide (MedChem Cat#HY-14658), Pomalidomide (MedChem Cat#HY-10984), Lenalidomide (MedChem Cat#HY-A0003), and Iberdomide/CC220 (MedChem Cat#HY-101291) were made into single-use aliquots at 10 mM in DMSO, stored at -80°C , and diluted. An equivalent proportion of Dimethyl Sulfoxide (DMSO) was added to all control samples.

Cell viability, differentiation, apoptosis, cell cycle and morphology analysis

Cell proliferation assays: MOLM13, MV4;11, OCI-AML-2 and IMSM2 cells were plated in 96-well plates. IMiD drug dilutions were made on a half-log scale and plated in

triplicate. Cells were split 1:10 on Days 3, 6, 9, 12, and 15 into fresh drug-containing media. Viable cells were measured using an LSR Fortessa (Becton Dickinson) every 3 days with DAPI used as viability stain. Cell counts were normalized to the DMSO control. Apoptosis was measured using the Annexin V Apoptosis Detection Kit (eBioScience Cat#88-8007074). For cell cycle analysis, cells were collected after indicated drug treatment, washed in PBS and fixed using the Cytofix/Cytoperm kit (BD Bioscience Cat#554714) prior to DAPI staining and analysis by flow cytometry. For assessment of differentiation, after indicated drug treatment or CRISPR/Cas9 modification, cells were stained with BV421-conjugated anti-CD11b (BioLegend Cat#301324) and APC-conjugated anti-CD14 (BioLegend Cat#367118), each at 5 uL antibody per 100 uL solution. Samples were then analysed on an LSR Fortessa flow cytometer. For morphology assessment, cells were collected after CRISPR-modification, centrifuged onto slides using the CytoCentrifuge (Thermo Scientific) and stained for microscopy using the JorVet DipQuick Stain (Jorgensen Laboratories, Inc. Cat#JO322). FLT3 cell surface expression assessed by flow cytometry using anti-CD135/FLT3/Flk-2 antibody (BioLegend Cat#313306) using 5 uL antibody per 100 uL solution.

Lentivirus production and CRISPR/Cas9-mediated cell modification

Sequences for selected small guide RNAs (sgRNAs) targeting human *IKZF1* and *MTA2* were extracted from the H1/H2 sgRNA libraries and additional sgRNAs were designed using the BROAD Genetic Perturbation Platform (GPP) web tool⁷³. Sequences used are listed in Supplementary Table 5. Oligonucleotides for sgRNAs were synthesized by Integrated DNA Technologies (IDT) and cloned into the lentiviral vector, improved-scaffold-pU6-sgRNA-EF1alpha_PURO-T2A-RFP (ipUSEPR) (Gift from Dr Yadira Soto-Feliciano and Dr. David Allis, Rockefeller University). Constitutive Cas9 expression was achieved using pLentiCas9-Blast (Addgene #52962). Lentivirus was produced in 293T cells following transient co-transfection with ipUSEPR or pLentiCas9 (10 µg), pMD2.G (3 µg) and psPAX2 (5 µg) per 10 cm tissue culture plate. Viral supernatant was collected at 24 and 48 h post transfection and passed through a 0.45 µm filter. Viral supernatant produced for pLentiCas9-Blast was concentrated approximately 30-fold by ultracentrifugation in an SW-28 rotor at 112,700g for 90 min. Viral supernatant for ipUSEPR was used neat. All human AML cell lines were transduced by co-incubation of 10⁵ cells with viral supernatant supplemented with polybrene 0.8µg/mL followed by centrifugation at 800g, 37°C for 2h. Cells infected with pLentiCas9-Blast were selected in Blasticidin 10 µg/mL for 6 days. For competition assays, Cas9-expressing human AML cell lines were infected with the respective sgRNA construct, were not sorted (yielding a mixed population of RFP+ and RFP- cells), and RFP expression was measured over time by flow cytometry. For assessment of proliferation, apoptosis and morphology, sgRNA-transduced cell populations were sorted using a FACSMelody Cell Sorter (BD) to produce a uniform population of high-RFP-expressing cells prior to commencing the assay; experiments were performed on bulk cell populations. For all experiments, a control non-targeting sgRNA construct was utilized for comparison (Supplementary Table 5).

Western blot analysis and protein immunoprecipitation

For Western blots, cells were collected, washed once in PBS and the protein was collected by lysis in 1X Laemmli buffer containing 10 mM DTT, sonicated and denatured for 5 min at 95°C. For MLL1/KMT2A, samples were loaded onto a 3–8% Tris-Acetate polyacrylamide gel (ThermoFisher) and separated by electrophoresis in 1X Tris-acetate running buffer (Novex#LA0041). Protein was then transferred to PVDF membrane using wet transfer in 1X Transfer Buffer (Novex#NP0006–1) containing 10% methanol for 2 h at 32V and 4°C. Western blotting for all other proteins was carried out using 10% Bis-Tris polyacrylamide gels and then transferred onto nitrocellulose membrane using the iBlot 2 Gel Transfer Device (ThermoFisher). The membranes were blocked in 5% milk in TBS-Tween buffer (TBST) for 1 hr and incubated overnight, as indicated, rabbit anti-IKAROS (Cell Signaling Cat#14859S) 1:1000 dilution, mouse anti-IKAROS (Invitrogen Cat#MA5–28613) 1:2000 dilution, anti-KMT2A/MLL1 (Bethyl Cat#A300–086A) 1:5000 dilution, anti-MENIN (Bethyl Cat#A300–105A) 1:5000 dilution, anti-HOXA9 (Abcam cat#ab140631) 1:5000 dilution, anti-MEIS1 (Abcam Cat#ab19867) 1:1000 dilution, anti-MTA2 (Abcam Cat#ab8106) 1:1000 dilution, anti-cMYC (Abcam Cat#ab32072) 1:1000 dilution, anti-BCL2 (Cell Signaling Cat#15071) 1:1000 dilution, anti-BCL-XL (Cell Signaling Cat#2764S) 1:1000 dilution, anti-MCL1 (Cell Signaling Cat#94296S) 1:1000 dilution, anti-Casein Kinase 1-alpha (Abcam Cat#ab108296) 1:1000 dilution, anti-Histone H3 (Abcam Cat#ab1791) 1:2500 dilution, anti-beta-ACTIN (Cell Signaling Cat#12620S) 1:1000 dilution, anti-LaminB1 (Abcam Cat#ab16048) 1:1000 dilution, or anti-GAPDH (Cell Signaling Cat#97166S) 1:1000 dilution, were used to immunostain the membrane. Membranes were washed in TBST >6 times and developed using a secondary HRP-linked anti-rabbit IgG, (Thermo Fisher Cat#45000682) 1:10000 or secondary HRP-linked anti-mouse IgG (Cell Signaling Cat#7076S) 1:2000 and chemiluminescence kit (Pierce). Precision Plus Dual Color Protein Standard (BioRad) was used to determine molecular weight. Blots were imaged using the ChemiDoc MP Imaging System (BioRad). Protein co-immunoprecipitation (Co-IP) was carried out using 20 million cells per Co-IP according to two different approaches, 1) *High salt nuclear extraction with NP40 wash*⁷⁴ (with modification): cells washed in PBS, then washed in hypotonic buffer (HB) (10 mM Tris pH 7.5, 10 mM KCl, 1.5 mM MgCl₂), then incubated for 10 min on ice in HB prior to dounce homogenization and centrifugation at 2600g 10 min, then resuspended in low salt buffer (LSB) (20 mM Tris pH 7.5, 12.5% glycerol, 1.5 mM MgCl₂, 0.2 mM EDTA pH 8.0), then an equal volume of high salt buffer (20 mM Tris pH 7.5, 12.5% glycerol, 1.5 mM MgCl₂, 0.2 mM EDTA pH 8.0, 1.2M KCl) is added dropwise while continuously mixing, then agitated at 4°C for 25min prior to centrifugation at 17,000g for 25min; the supernatant containing extracted protein is then diluted 4-fold in LSB prior to proceeding with immunoprecipitation. The resulting protein extract was then incubated with antibody-bound beads at 4°C (as described below). After overnight incubation, protein-bound beads were then washed three times in wash buffer (20 mM Tris pH 7.5, 150 mM NaCl, 0.25% NP40, 0.2 mM PMSF). 2) *High glycerol wash*⁷⁵: cells were collected and washed in PBS, then incubated in nuclear lysis buffer (50 mM KCl, 10 mM MgSO₄·7H₂O, 5mM HEPES, 0.05% NP40, 1mM PMSF, 3mM DTT, supplemented with Complete protease inhibitor), followed by wash of nuclei in nuclei wash buffer (NaCl 300mM, Tris pH7.5 50mM, MgCl₂ 1mM) and subsequent disruption using dounce homogenization in buffer EB300 (Tris pH

7.5 50 mM, EDTA 1 mM, NP-40 1%, NaCl 300mM) and centrifugation at 17,000g for 15min. The resulting nuclear extract was supplemented with 250U benzonase (Sigma) and then incubated with antibody-bound beads overnight at 4°C. Protein-bound beads were washed in buffer BC200 (20 mM Tris (pH 7.9), 0.2 mM EDTA, 1 mM DTT, 0.2 mM PMSF, 20% glycerol, and 200 mM of KCl) three times. In both protocols, protein was eluted from beads by incubating in 1X Laemmli buffer at 95°C for 10 min prior to Western blot analysis. Immunoprecipitation of each protein of interest carried out using 5 µg antibody with Protein A Dynabeads (for rabbit antibody) or Protein G Dynabeads (for mouse antibody). Beads washed three times (0.5% Bovine serum albumin, Triton X-100 0.05% in PBS) and incubated with antibody overnight with constant turning; 5µg of antibody was used for each IP. Beads washed again three times prior to addition of protein preparation. Anti-bodies used were: MENIN antibody (Bethyl), IKAROS antibody (Invitrogen-mouse antibody), KMT2A/MLL1 antibody (Bethyl), normal rabbit IgG control (Bethyl), or normal mouse IgG control (Cell Signaling). All buffers were supplemented with 1X Complete protease inhibitor tablets (Roche#11836145001).

RNA isolation, quantitative real-time PCR and RNA-seq

For all cell line experiments, RNA was isolated from cells following the indicated drug treatments using the RNeasy Mini Kit (Qiagen). RNA samples from *in vivo* experiments were obtained by isolating human cells from mouse marrow using the EasySep mouse-human chimera kit (Stem Cell Technologies) followed by RNA extraction using the PicoPure RNA isolation kit (Thermo Fisher). For RT-qPCR, cDNA synthesis was carried using the Azuraflex cDNA Synthesis Kit (Azura Genomics). Taqman gene expression assay for *BCL2* (ThermoFisher Cat #4331182) and *MYC* (ThermoFisher Cat #4331182) was used for RT-qPCR reaction on the ViiA 7 Real-Time PCR system (Applied Biosystems). *GAPDH* was used a housekeeping control. For next-generation RNA-sequencing, RNA quality was assessed using the Agilent TapeStation 4200 (Agilent Technologies). Library preparation was performed using the NEBNext Ultra II RNA Library Prep Kit for Illumina (New England Biolabs). Sequencing was performed on an Illumina Nextseq 550 (Illumina) acquiring 37 bp, paired-end reads.

Chromatin immunoprecipitation and next-generation sequencing (ChIP-seq)

ChIP-seq was performed in MV4;11 and MOLM13: cells were crosslinked in 1% methanol-free formaldehyde (ThermoFisher) for 7 min at room temperature followed by quenching of the formaldehyde using 100 mM Tris pH 8.0 and 250 mM Glycine. Cells were then lysed using 50 mM Tris-HCl pH 8.0, 100 mM NaCl, 5 mM EDTA, 1% SDS for 10 min at ambient temperature and chromatin was collected by centrifugation at 10,000 3xg for 10 min. Chromatin was then resuspended in 66mM Tris-HCl pH 8.0, 100mM NaCl, 5mM EDTA, 1.7% Triton X-100, 0.5% SDS and sheared using an E100S sonicator (Covaris) to chromatin fragments of 200–400 base-pair DNA size. Sheared chromatin from the 20 million cells was used in each immunoprecipitation using the respective antibodies: anti-MENIN (Bethyl Cat#A300–105A), KMT2A/MLL1 (Bethyl Cat#A300–086A), MEIS1 (Abcam Cat#ab19867) and IKAROS (Cell Signaling Cat#14859S) antibodies and protein-A magnetic beads (Dyna). Immunoprecipitated DNA fragments were eluted and de-crosslinked in 100 mM NaHCO₃, 100 mM NaCl, 1% SDS, and quantified by

TapeStation 4200 (Agilent) and Qubit (ThermoFisher). 1–10 ng of DNA was used in preparation of Illumina compatible libraries using SMARTer ThruPLEX DNA-Seq Kit (Takara) followed by sequencing using NextSeq550 (Illumina) to obtain paired-end reads (R1: 37bp, R2: 37bp).

CUT&RUN sequencing

The protein-A-MNase fusion protein (pA-MNase) was produced by transforming the pK19pA-MN plasmid (Addgene #86973) into Rosetta (DE3) competent cells (Novagen). Expression of the pA-MNase was induced in liquid LB culture at an optical density of 0.7 with IPTG treatment for 2 h. Following cell lysis, pA-MNase was purified using IgG Sepharose 6 Fast Flow beads (GE Healthcare Cat#17–0969-01) followed by concentration in a 20,000 MW Slide-A-Lyzer cassette (Thermo Fisher #66012). The pA-MNase product was assessed by BCA quantification and Western blot analysis. CUT&RUN was performed as previously described⁴². In short, 5×10^5 cells were washed twice in PBS, then once in a wash buffer (20mM HEPES pH 8.0, 150mM NaCl, 0.5mM spermidine) followed by immobilization on Concanavalin A magnetic beads activated in binding buffer (20mM HEPES pH 8.0, 10mM KCl, 1mM CaCl₂, 1mM MnCl₂) (Polyscience). The immobilized cells were permeabilized by washing in wash buffer supplemented with 0.1% Triton-X100 and incubated with anti-IKAROS antibody (Cell Signaling Cat#14859S), rabbit IgG control (Bethyl Cat#P120–201), anti-CTCF (Cell Signaling Cat#3418S) or anti-H3K27Ac (Diagenode Cat#15410196) at 4°C with addition of EDTA to 2mM. After 2-hour incubation the cells were washed twice and incubated with Protein-A-MNase conjugate at 4°C. After 4 h, the cells were washed twice and MNase was activated by addition of CaCl₂ to 20mM. The DNA digestion was stopped by addition of EDTA and EGTA, both to 10mM. DNA fragments were collected in supernatant and purified using 1.8x AMPure XP beads (Beckman Coulter) which were then converted to Illumina compatible libraries using NEBNext Ultra II DNA Library Prep Kit for Illumina (New England BioLabs) followed by sequencing using NextSeq550 (Illumina). For the drug treatment experiment, carry-over *E.coli* DNA from the pA-MNase preparation was used for sample normalization during bioinformatic analysis.

ATAC-sequencing

Five million cells from MV4;11 and MOLM13 were washed in PBS and resuspend in a hypotonic buffer (50 mM KCl, 10 mM MgSO₄, 5 mM HEPES, 0.05% NP-40, 1 mM PMSF, 3 mM DTT) to generate intact nuclei and washed three times in a nuclear wash buffer (10 mM Tris HCl pH 7.5, 10 mM NaCl, 3 mM MgCl₂). 50,000 nuclei per cell line were used for the transposition reaction. Nuclei were incubated in 1X TD Buffer (Illumina) and 2.5 μM Transposase enzyme (Illumina) for 30 minutes at 37 °C. Transposed DNA was then extracted from nuclei using the MiniElute PCR purification Kit (Qiagen). Transposed DNA fragments were amplified using NEBNext® High-Fidelity PCR kit (NEB) with a universal Nextera primer and a unique indexing primer and sequenced using NextSeq550 (Illumina) obtaining paired end reads (R1: 75bp; R2: 75bp) with 57 million and 48 million reads obtained for the MOLM13 and MV4;11 cell lines, respectively.

Sample preparation for quantitative mass spectrometry based global protein measurements

Ten million cells from each cell line (MV4;11, MOLM13 and OCI-AML2) were treated with DMSO, thalidomide 10 μ M, lenalidomide 5 μ M, pomalidomide 1 μ M or iberdomide/CC220 0.1 μ M for 5 h and cells were harvested by centrifugation and washed three times in PBS. For combination drug treatment, cells were first treated in DMSO or VTP-50469 50 nM for 5 days prior to IMiD treatment. Lysis buffer (8 M Urea, 50 mM NaCl, 50 mM 4-(2-hydroxyethyl)-1-piperazineethanesulfonic acid (EPPS) pH 8.5, Protease and Phosphatase inhibitors) was added to the cell pellets and manually homogenized by 20 passes through a 21-gauge (1.25 in. long) needle and resulting cell lysate was clarified by centrifugation. Bradford assay (Bio-Rad) was used to determine protein concentration. 200 μ g of protein for each sample was reduced, alkylated, LysC/Trypsin digested and TMT labelled as previously described⁴⁰. Each of the sample channels were combined in a 1:1 ratio, desalted using C18 solid phase extraction cartridges (Waters) and analysed by LC-MS/MS for quality control analysis and channel ratio comparison. Equally combined samples were then offline fractionated into 96 fractions by high pH reverse-phase HPLC (Agilent LC1260) through an aeris peptide xb-c18 column (phenomenex) with mobile phase A containing 5% acetonitrile and 10 mM NH_4HCO_3 in LC-MS grade H_2O , and mobile phase B containing 90% acetonitrile and 5 mM NH_4HCO_3 in LC-MS grade H_2O (both pH 8.0) and resulting fractions were then pooled into 24 fractions, desalted, and submitted for mass spectrometry analysis.

Sample preparation for BioID interaction analysis

To generate BioID systems, coding sequences for IKAROS, MEIS1, HOXA10, and ZNF692 were synthesized and cloned by Twist Biosciences to produce N- and C-terminally BirA* tagged pTwist-Lenti-SFFV-Puro-WPRE constructs. Stably expressing MV4;11 and MOLM13 cell lines were then generated and the near-equal biotin labelling was determined by Western blotting with streptavidin-HRP (data not shown) and N-terminally BirA* tagged IKAROS, C-terminally BirA* tagged MEIS1, C-terminally BirA* tagged HOXA10 and C-terminally BirA* tagged ZNF692. MV4;11 and MOLM13 cell lines were chosen for subsequent experiments. Cell lines were expanded to large volumes and 50 μ M Biotin was added to culture medium 24 h prior to harvest. Cells were harvested and washed 3 times with PBS and then resuspended in a hypotonic buffer (50 mM KCl, 10 mM MgSO_4 , 5 mM HEPES, 0.05% NP-40, 1 mM PMSF) followed by 3 washes in a nuclear wash buffer (10 mM Tris HCl pH 7.5, 10 mM NaCl, 3 mM MgCl_2) to generate intact nuclei. Nuclei were lysed in BioID Lysis buffer (50 mM Tris, pH 7.5, 500 mM NaCl, 0.4% SDS, 2% Triton X-100 supplemented with Roche protease inhibitor tablets), followed by probe tip sonication (3 rounds, duty cycle 65%, 30 s pulses). Samples were clarified by centrifugation and lysates were quantified by bicinchoninic acid (BCA) assay. Ten mg of protein per replicate, two replicates per cell line, were incubated with 80 μ L of streptavidin sepharose high performance beads (Millipore Sigma) overnight at 4 $^\circ\text{C}$. After incubation beads were washed with 2 mL of 2% SDS, 2 mL of BioID lysis buffer three times, 10 mL of 50 mM Tris six times, and 5 mL of 50 mM triethylammonium bicarbonate (TEABC) once. Streptavidin bound proteins then underwent on-bead tryptic digestion by adding 1 μ g of sequencing grade trypsin (Promega) and incubating beads overnight at 37 $^\circ\text{C}$. After

digestion, the supernatant was separated from the streptavidin beads and acidified to 1% Formic acid. Acidified peptides were then de-salted and purified using SOLA μ ™ Solid phase extraction plates (Thermo Fisher Scientific).

Mass spectrometry data collection

All mass spectrometry data were collected using an Orbitrap Fusion Lumos mass spectrometer (Thermo Fisher Scientific, San Jose, CA, USA) coupled with a Proxeon EASY-nLC 1200 LC pump (Thermo Fisher Scientific). Peptides were separated on an EasySpray ES803a 75 μ m inner diameter microcapillary column (Thermo Fisher Scientific). For global quantitative proteomics and BioID interaction proteomics, peptides were separated using a 190 min/140 min gradient of 6 – 27%/5 – 34% buffer B (95% acetonitrile) in 1.0% formic acid with a flow rate of 300 nL/min, respectively. For global quantitative proteomics, each analysis used a MS3-based TMT method as described previously⁷⁶. For global quantitative proteomics and BioID interaction proteomics the data were acquired using a mass range of m/z 340 – 1350/375 – 1500, resolution 120,000, AGC target 5×10^5 , maximum injection time 100/50 ms, dynamic exclusion of 120 seconds for the peptide measurements in the Orbitrap, respectively. For global quantitative proteomics and BioID interaction proteomics, data dependent MS2 spectra were acquired in the ion trap with a normalized collision energy (NCE) set at 35%, AGC target set to $1.8 \times 10^4/4 \times 10^5$ and a maximum injection time of 120/50 ms, respectively. MS3 scans were acquired in the Orbitrap with HCD collision energy set to 55%, AGC target set to 2×10^5 , maximum injection time of 150 ms, resolution at 50,000 and with a maximum synchronous precursor selection (SPS) precursors set to 10. For BioID interaction proteomics, data dependent MS/MS spectra were acquired in the ion trap in centroid mode with the collision energy set at 30%, AGC target set to 1×10^4 and a maximum injection time of 30 ms.

Mass spectrometry data analysis

Proteome Discoverer 2.2 (Thermo Fisher Scientific) was used for .RAW file processing and controlling peptide and protein level false discovery rates, assembling proteins from peptides, and protein quantification from peptides. MS/MS spectra were searched against a Swissprot human database (December 2016) with both the forward and reverse sequences. For BioID data searches a FASTA entry was included for the protein sequence of BirA*. Database search criteria was conducted as previously described.⁷⁵ Reporter ion intensities were normalized and scaled using in-house scripts in the R framework (R Development Core Team, 2014). Statistical analysis was carried out using the limma package within the R framework (Ritchie et al., 2015). For BioID data spectral counting analysis, individual Proteome Discoverer searches were conducted on IKAROS, MEIS1 and HOXA10 BioID .RAW files, combining both replicates. The protein identities and their corresponding PSM values were then merged between MV4;11 and MOLM13 cell lines to create a unified dataset with proteins uniquely detected in MV4;11 or MOLM13 cells excluded. The protein identities were then referenced against the CRAPome repository⁷⁷ to remove contaminants common to affinity purification MS experiments. The dataset was further filtered by removal of proteins that met either of the following two criteria; if the number of “experiments detected” in the CRAPome repository was greater than the average of the number of “experiments detected” values across our BioID datasets or if the

“average spectral count” reported in the CRAPome repository was greater than the average of the “average spectral count” values detected in our BioID datasets. NuRD complex member proteins are highly prevalent in the CRAPome and because of the biological relevancy of this study, we made a special exemption for removal. After CRAPome proteins were removed, the resulting proteins were ranked by descending number of PSMs and plotted in rank order. For Label Free Quantitation (LFQ), analysis was carried out using Proteome Discoverer 2.2. Separate analyses were made for MV4;11 and MOLM13 cells using corresponding IKAROS, MEIS1, HOXA10 and ZNF692 BioID .RAW files that were searched together and the Minora Feature Detector was used to generate abundance values for proteins across the different samples. Normalization was applied in the Precursor Ions Quantifier tool using the Total Peptide Amount feature. Retention time alignment was set at 15 minutes. Log₂ abundance ratios were generated for IKAROS, MEIS1 and HOXA10 over ZNF692 and a threshold was set to define enrichment as being greater than 2-fold (Log₂ ratio=1). Based on Western blot analysis and the median value of Log₂ ratios called in the MOLM13 experiment (IKAROS/ZNF692=-1.64, MEIS1/ZNF692=-0.73, and IKAROS/ZNF692=-1.95) we concluded that ZNF692-BirA* induced significantly higher labelling than IKAROS/MEIS1/HOXA10. Thus, MOLM13 BioID data was further normalized by subtracting the median value of all Log₂ ratios in each comparison from each individual value. No extra normalization was applied to the MV4;11 LFQ data. PSM values from individual searches described above were added, and any protein with less than 2 PSMs was excluded from the LFQ analysis. Of those proteins that had 1 or more isoform detected, the isoform with the most PSMs was retained and the others were removed.

BH3 profiling

BH3 profiling was done as described previously⁴⁶. Cells were permeabilized with 0.001% digitonin suspended in MEB2 buffer (150 mM mannitol, 10 mM HEPES-KOH pH 7.5, 150 mM KCl, 1 mM EGTA, 1 mM EDTA, 0.1% BSA, 5 mM succinate) and treated with different BH3- only peptides in 384-well plate. After 60mins incubation at 25°C, cells were fixed with 4% formaldehyde for 10 mins at RT followed by neutralization by adding N2 buffer (1.7 M Tris base, 1.25 M glycine, pH 9.1). Cells were stained overnight at 4°C with Hoechst 33342 (H3570, Invitrogen) and anti-cytochrome c-Alexa Fluor 488 (6H2.B4/612308). The rate of loss of cytochrome c was analysed using Intellicyt iQue flow cytometer in response to each BH3 peptide. Assay were conducted in triplicates. DMSO and alamethicin were used as negative and positive control for cytochrome c release.

IKAROS overexpression cell lines

IKAROS overexpression vectors were a kind gift from Dr. William G. Kaelin and Dr. Vidyasagar Koduri, Dana-Farber Cancer Institute: 1. Wild type IKAROS overexpression vector (CAG-*IKZF1*-WT-FLAG-IRES-GFP, <https://www.addgene.org/107387/>), 2. Non-degradable mutant IKAROS overexpression vector (CAG-*IKZF1-V1-Q146H*-FLAG-IRES-GFP; <https://www.addgene.org/69048/>), and 3. Empty vector control (pLKO5-GFP, <https://www.addgene.org/57822/>). Lentivirus produced as described above. The MOLM13 cell line was transduced as described above and sorted using a FACSMelody Cell Sorter (BD) to produce a uniform population of GFP-expressing cells.

Human CD34+ cell isolation and MLL-AF9 transduction

Production of MLL-AF9 transduced human CD34+ cells has been described.⁷⁸ Human CD34+ cells were isolated from human cord blood (New York Blood Center) using the EasySep™ Human Cord Blood CD34 Positive Selection Kit II (Stemcell Technologies). For pre-enrichment, Lymphoprep (Stemcell Technologies) and SepMate™ columns (Stemcell Technologies) were used. Viral supernatants were generated by co-transfection of HEK293-T cells with retroviral (pMSCV-MLL-AF9-IRES-GFP)⁷⁸ expression vector with packaging and envelope vectors (Human Retro: pUMVC and VSV-G) and X-tremeGene transfection reagent (Millipore). The viral supernatant was filtered through 0.45µm and was concentrated using Amicon Ultra centrifugal filters (Millipore). Human CD34+ cells were plated on retronectin-coated plates (Takara) and were spin infected at a 1:1 dilution of virus:media at 800g at 37°C for 1.5h. The cells were dissociated from the plates using enzyme-free dissociation buffer (Gibco) and were plated in fresh media. Cells were maintained in IMDM with 20% FBS, 1x penicillin/streptomycin (Gibco), 1xβ-mercaptoethanol (Gibco), 6 µg/mL hIL3, 10 µg/mL hIL6, 10 µg/mL hSCF, 10 µg/mL TPO, and 10 µg/mL FLT3 (Stemcell Technologies) at 37°C and 5% CO₂. Two days after transduction, GFP positive cells were sorted using FACSAria cell sorter (BD Bioscience).

Colony-formation assay

Colony-forming unit (CFU) assays were performed by plating 200 MOLM-13 CRISPR-modified cells into 3 mL Methocult GF M3434 (STEMCELL Technologies). For each *sgRNA*, four separate methylcellulose plates were used. Colonies were quantified 9 and 12 days after plating by manual counting. On the 13th day of the experiment, each plate was washed with PBS, cells were spun down and resuspended in quadruplicate to run on LSR Fortessa to quantify cells per plate.

Statistical Analysis and Reproducibility

No statistical methods were used to pre-determine sample sizes but our sample sizes are similar to those reported in previous publications²⁴. Single experiments shown are representative of at least 3 independent experimental replicates. Data collection and analysis were not performed blind to the conditions of the experiments. For PDX studies, animals were randomized according to weight and leukaemia burden prior to treatment using Excel (Microsoft). Animals injured by gavage and required to be sacrificed were excluded from the analysis. For proliferation assays, dose-response curves were calculated in a variable slope model as a four-parameter dose-response curve (GraphPad Software). Absolute IC₅₀s were calculated by setting the maximal inhibition baseline parameter to 0% and constraining the minimal inhibition top parameter to 100%. The calculation was done via non-linear regression of the log of the dose (GraphPad Software). Kaplan-Meier survival curves and paired T-test were performed using the statistical software, GraphPad PRISM. Gene set enrichment analysis (GSEA v3.0 software/Broad Institute)^{79,80} was used to identify functional associations from the described RNA-seq profiles. Global analysis was performed on raw RNA-seq counts; specific query of gene sets of interest was performed in “pre-ranked” mode using gene lists ranked according to DESeq statistical z-score. Significance cut-offs were assessed on the basis of the GSEA standard recommendations: absolute NES

1, $P < 0.05$, Benjamini–Hochberg FDR < 0.25 . Gene sets used in presented data are listed in Supplementary Table 6. Bliss independence and Loewe additivity models were used to assess synergy, as described previously⁸¹. The Bliss independence model calculates a quantitative measure, called the excess over Bliss, which represents the difference between the observed combined effect and the expected combined effect of the two compounds. The Chou-Talalay combination index for the Loewe additivity model is a dose-effect approach to estimate the effect of combining two compounds based upon the dose of each individual compound that produces the same quantitative effect. All data from flow cytometry was analysed using Flojo software, Becton Dickinson (v10.6.2).

Bioinformatics Analysis

Raw Illumina sequencer output was converted to FASTQ format using bcl2fastq (v2.20.0.422) (Illumina, Inc.). Reads (paired-end 37-mers) were aligned to the human genome (hg19) using STAR (v2.7.5a)⁸², sorted and duplicates marked/removed with picard pipeline tools (v2.9.4). Final “deduped” .BAM files were indexed using SAMtools (v1.95)⁸³. Files for data visualization were produced using IGVtools (TDF signal pileups; v2.3.75)⁸⁴ and ngs.plot (pileup heatmaps; ChIP-seq only). ChIPseq signal peaks were called using MACS2 (v2.1.4). For RNA-seq, raw counts were calculated with HTSeq (htseq-count, v0.11.2)⁸⁵. Raw counts were used to calculate differential expression values with the R Bioconductor DESeq2 package (v1.24.0)⁸⁶. Results were filtered to exclude non-protein-coding genes (based on Ensembl gene biotype annotations) and low-expressed genes (those with average values < 1 in rlog scale for both treatments in comparison). Expression differentials with adjusted pValue < 0.05 were considered significant with the additional requirement of a greater than two-fold change, where indicated. RNA-seq data were further analysed through the use of Ingenuity Pathway Analysis (IPA) (QIAGEN Inc., <https://www.qiagenbioinformatics.com/products/ingenuitypathway-analysis>). For CUT&RUN-seq analysis, FASTQ files were processed using a version of the published CUT&RUNTools suite⁴⁴ (release date 19th August, 2019), modified to run on a local computer cluster. Briefly, reads were trimmed using trimmomatic and aligned to the human genome (hg19) with Bowtie2 (v2.3.4.3)⁸⁷. Resulting BAM files were sorted, duplicates marked and filtered for fragments < 120 bp (all with SAMtools, v1.95), and peaks called (with MACS2, v2.1.4). ATAC-seq data was processed as described above for ChIPseq. Enhancer prediction using the activity-by-contact model (ABC) was carried out as previously described⁴⁵. Heatmap displays for RNA-seq data were generated using the Bioconductor package ComplexHeatmap (v3.14)⁸⁸ using RStudio (v1.4.1106) with R (v3.6.0). GNU parallel (v20161222)⁸⁹ was used to facilitate simultaneous processing and analysis of samples.

Publicly Available Data Usage

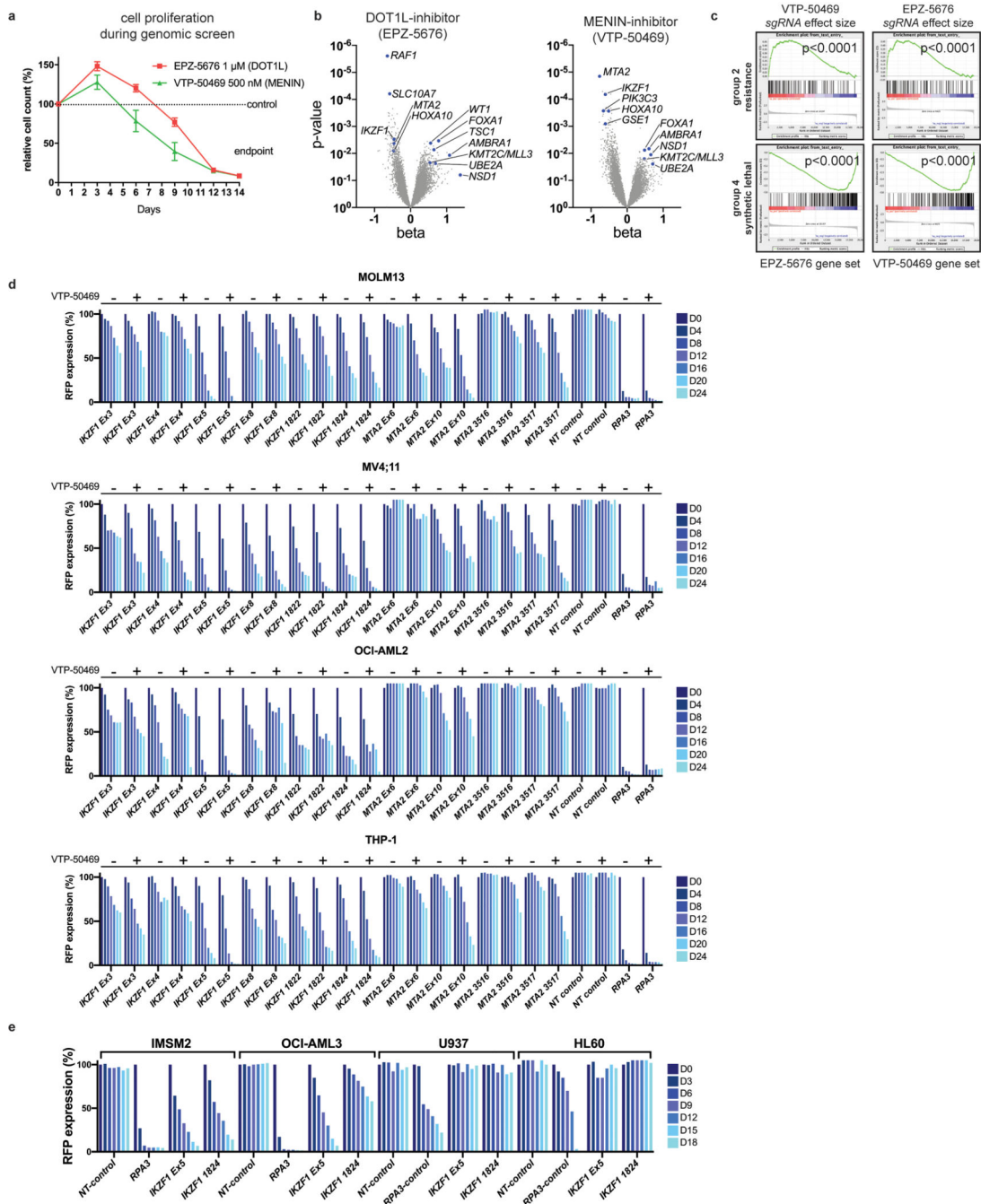
The Cancer Dependency Map (DepMap) from the Broad Institute of MIT and Harvard, Boston, MA, USA,³⁵ was used to examine cancer dependencies on *IKZF1*, *MEN1*, *DOT1L* and *ZFP91* (Broad(2021): DepMap21Q4Public. figshare.Dataset doi:[10.6084/m9.figshare.12280541.v3](https://doi.org/10.6084/m9.figshare.12280541.v3)). The cBio Cancer Genomics Portal (cBIOPortal)^{34,90} was used to examine *IKZF1* gene expression across a range cancer subtypes utilizing data from The Cancer Genome Atlas (TCGA) (<https://www.cancer.gov/tcga>). For ABC enhancer predictions, average Hi-C matrix data was utilized, as recommended⁴⁵, and obtained from

the Broad Institute of MIT and Harvard (<https://github.com/broadinstitute/ABC-Enhancer-Gene-Prediction>) as well as an additional publicly available HiC dataset for MV4;11⁹¹.

Data Availability

Raw and analysed data for ChIP-seq, CUT&RUN-seq, RNA-seq, ATAC-seq and ABC model predictions have been deposited at the National Center for Biotechnology Information (NCBI) Gene Expression Omnibus (GEO) under the accession number GSE168463; deposited data correspond to Figures 3, 4, 5, 6, 7 and associated extended data figures. All mass spectrometry data and search results have been deposited to the ProteomeXchange Consortium (<http://proteomecentral.proteomexchange.org/cgi/GetDataset?ID=PXD007862>) via the PRIDE partner repository with the data set identifiers PXD025227, PXD025228, PXD025229, PXD025230, PXD025231, PXD025232, PXD025271 and PXD025272. Additional data that support the findings of this study are available from the corresponding author upon reasonable request.

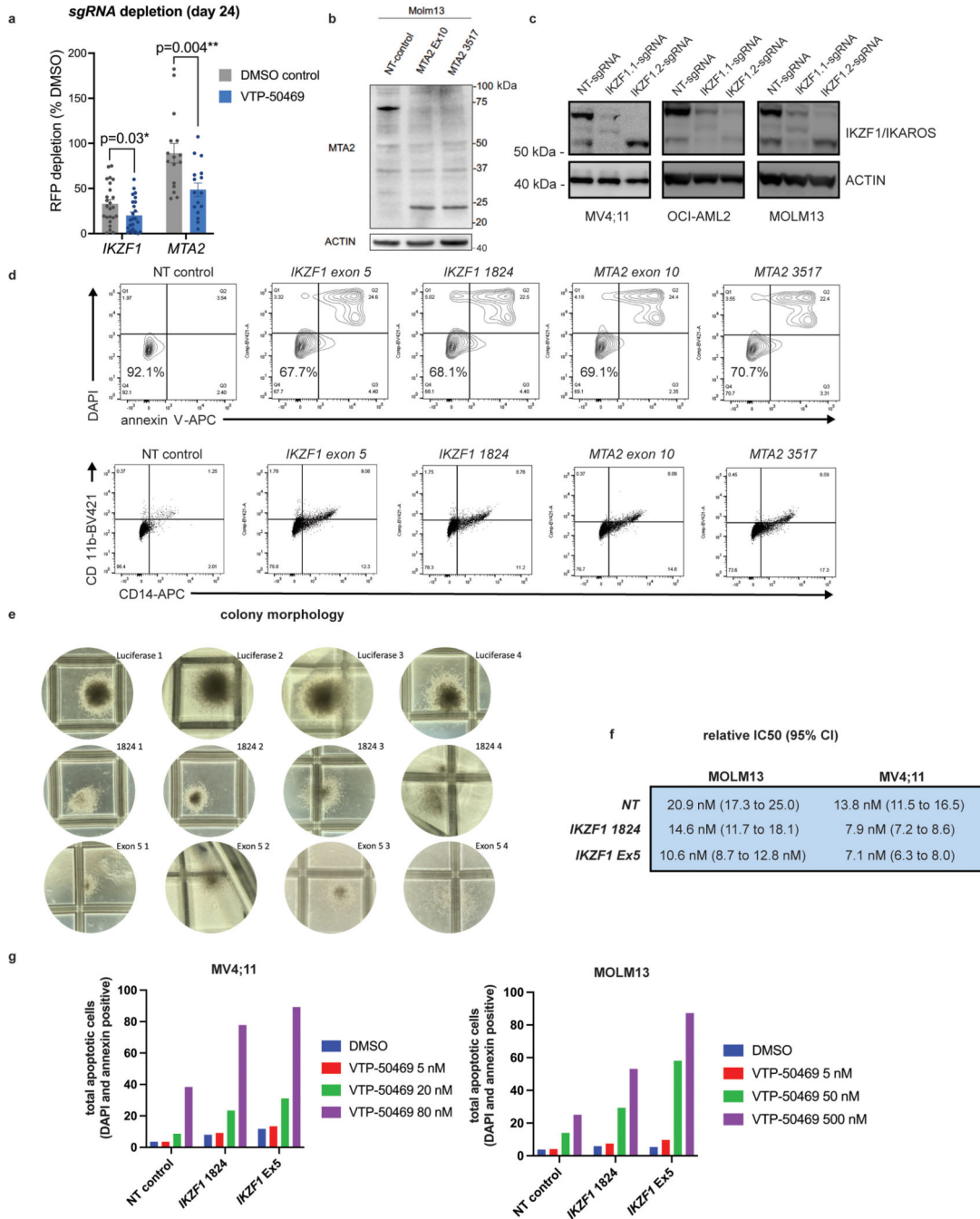
Extended Data



Extended Data Fig. 1. Chromatin remodeling complexes modulate the cellular response to therapeutic targeting of *MLL-r* driven gene expression.

a. Proliferation assay conducted in real-time during the functional genomic screen showing cell number over time. Data represent mean \pm SEM (n=4). **b.** Volcano plots depicting Wald p-value and beta value calculated using MAGeCK MLE for VTP-50469 and EPZ-5676, comparing the vehicle-treated and drug-treated state on Day 14. **c.** Gene set testing comparing the behaviour of group 2 (resistance) and group 4 (synthetic lethal) genetic hits

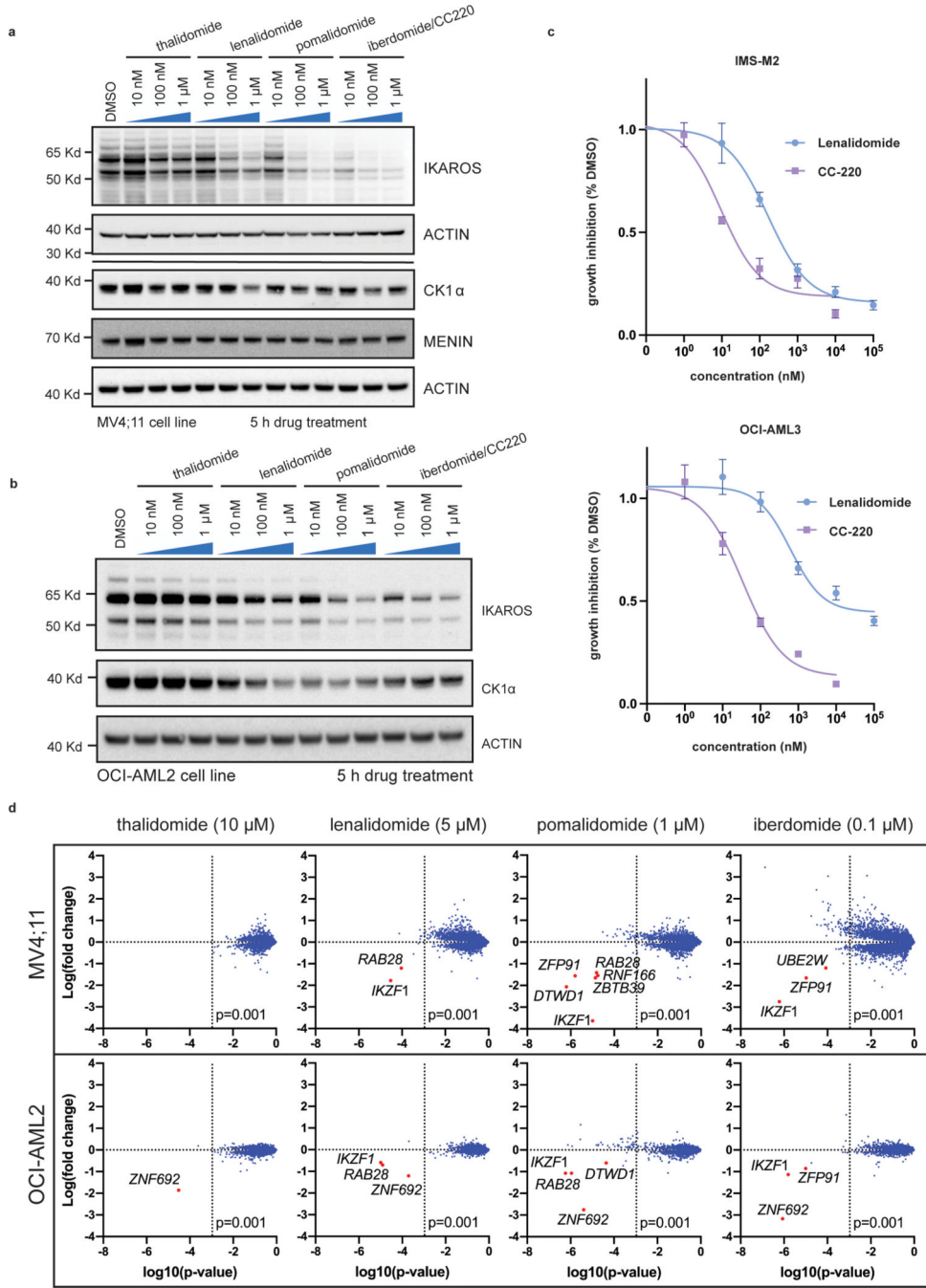
between each screen. Family-wise error rate p-value determined by GSEA computational method. **d**, Expanded panels of CRISPR/Cas9-based competition assays targeting either *IKZF1* or *MTA2* monitoring *sgRNA*-RFP expression over time in Cas9-expressing in 4 *MLL-r* human AML cell lines (MOLM13, MV4;11, OCI-AML2 and THP-1), with and without concurrent treatment with the MENIN inhibitor, VTP-50469. **e**, CRISPR/Cas9-based competition assays targeting *IKZF1* monitoring *sgRNA*-RFP expression over time in 4 non-*MLL*-fusion human AML cell lines (IMSM2, OCI-AML3, U937 and HL60) expressing Cas9. IMSM2 and OCI-AML3 carry the *NPM1c* mutation.



Extended Data Fig. 2. Using CRISPR/Cas9 to genetically target *IKZF1* and *MTA2* and validate genomic screen findings.

a. Combined analysis of sgRNA depletion across samples, depicted in Extended Data Fig. 1d, showing enhanced sgRNA depletion in the presence of the MENIN-inhibitor, VTP-50469, despite the disadvantage of drug-induced cell cycle arrest. Data represent mean \pm SEM with p-value by two-tail t-test evaluated for n=4 cell lines and n=6 sgRNAs targeting *IKZF1* or n=4 sgRNAs targeting *MTA2*. **b.** Western blot analysis for *MTA2* protein in sgRNA-RFP sorted cells comparing *MTA2*-targeted bulk cell populations with

non-targeting control and ACTIN used as a loading control. **c**, Western blot analysis for IKAROS protein in sgRNA-RFP sorted cells comparing *IKZF1*-targeted bulk cell populations with non-targeting control and ACTIN used as loading control. **d**, Analysis of annexin V staining (apoptosis) and CD11b/CD14 (monocytic differentiation) using flow cytometry 7 days following CRISPR/Cas9-mediated deletion of either *IKZF1* or *MTA2*. Representative experiment is shown. **e**, Colony forming assay comparing MOLM13 cells with sgRNA targeting *Luciferase* (Non-Targeting) control versus two different sgRNAs targeting *IKZF1* (n =4 per sgRNA), representative colony morphology is shown. **f**, Relative IC₅₀ for proliferation assays, pertaining to Fig. 1j, comparing MOLM13 cells with sgRNA targeting *Luciferase* (Non-Targeting control) and two sgRNAs targeting *IKZF1* (n=3 per sgRNA) upon treatment with MENIN inhibition. **g**, Apoptosis assay in MOLM13 and MV4;11 cell lines testing the impact of *sgRNAs* targeting *Luciferase* (NT control) versus two sgRNAs targeting *IKZF1* on the response to MENIN inhibition with VTP-50469, using doses indicated. Apoptosis was assessed by DAPI exclusion (viability) and annexin V staining with 50,000 cells analysed per sample. Representative example of multiple independent experiments.



Extended Data Fig. 3. IMiDs effectively target IKAROS protein for degradation in human *MLL-r* AML.

a, Western blot analysis for IKAROS, CK1α and MENIN protein following treatment of MV4;11 human *MLL-r* AML cell line for 5 hours with increasing doses of THAL, LEN, POM and CC220, using ACTIN as a loading control. **b**, Western blot analysis for IKAROS and CK1α following treatment of OCI-AML2 human *MLL-r* AML cell line for 5 hours with increasing doses of THAL, LEN, POM and CC220, using ACTIN as a loading control. **c**, LEN and CC220 dose-response curves on: Day 9 of treatment for

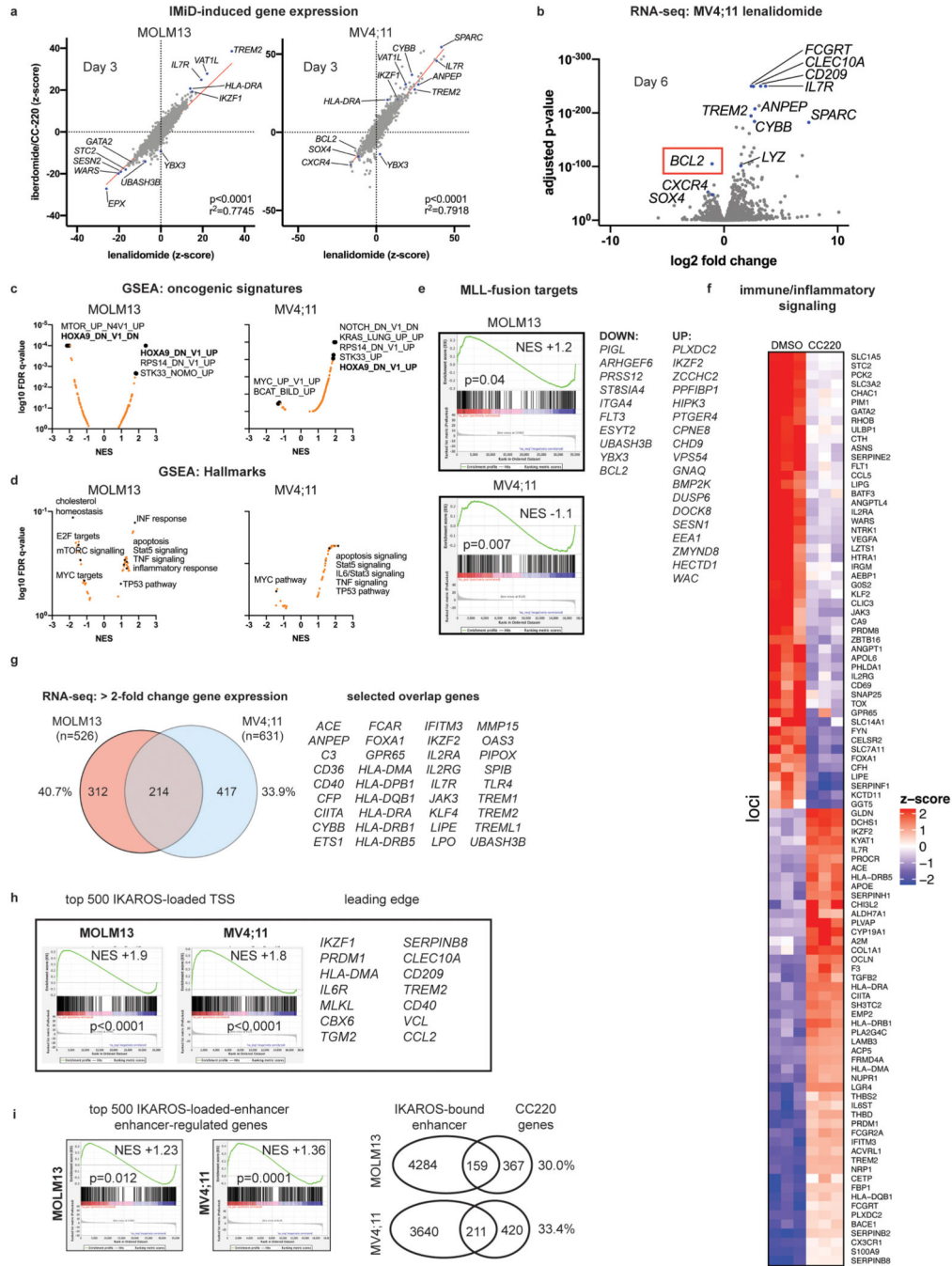
the *NPM1*-mutant (*NPM1c*) IMSM2 human AML cell line cell (Absolute IC₅₀ 267.0 nM [95% CI 189.6 to 381.0] for LEN, 17.3 nM [95% CI 9.3 to 37.8] for CC220) and Day 18 of treatment for the *NPM1*-mutant (*NPM1c*) OCI-AML3 human AML cell line (Absolute IC₅₀ 4626 nM [95% CI could not be calculated] for LEN, 57.7 nM [95% CI 33.1 to 101.5] for CC220). Data represent mean+/-SEM with absolute IC50 indicated (n=3). **d**, Scatterplot for MS determination of IMiD substrates 5 hours after drug treatment in the MV4;11 and OCI-AML2 cell lines. Data represent the log-fold change in abundance and log₁₀(p-value). p-value determined by moderated t-test as implemented by the Bioconductor Limma package.

Author Manuscript

Author Manuscript

Author Manuscript

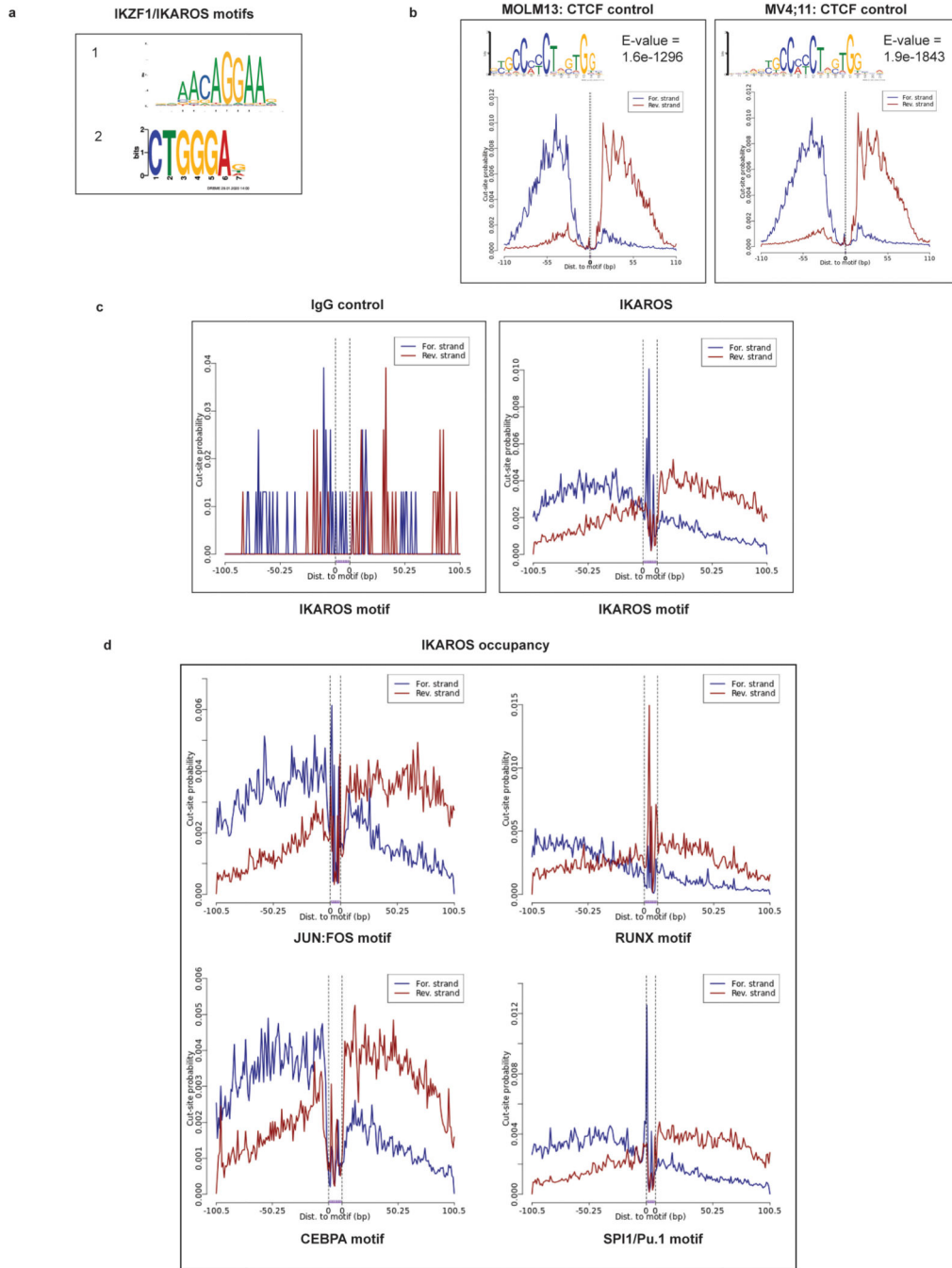
Author Manuscript



Extended Data Fig. 4. IKAROS degradation perturbs diverse cellular pathways.

a, RNA-seq dot-plot with linear regression showing z-score for differential gene expression correlating LEN (5 μ M) and CC220 (1 μ M) treatment for 3 days. **b**, RNA-seq volcano plot for MV4;11 treated with LEN for 6 days. **c**, GSEA results for “oncogenic signatures” for RNA-seq data on Day 3. Dot plot is shown of the log₁₀ false discovery rate (FDR) q-value and normalized enrichment score (NES) as determined by GSEA computational method. **d**, GSEA results for “Hallmarks” signatures. Dot plot is shown of the log₁₀ false discovery rate (FDR) q-value and normalized enrichment score (NES) as determined by the

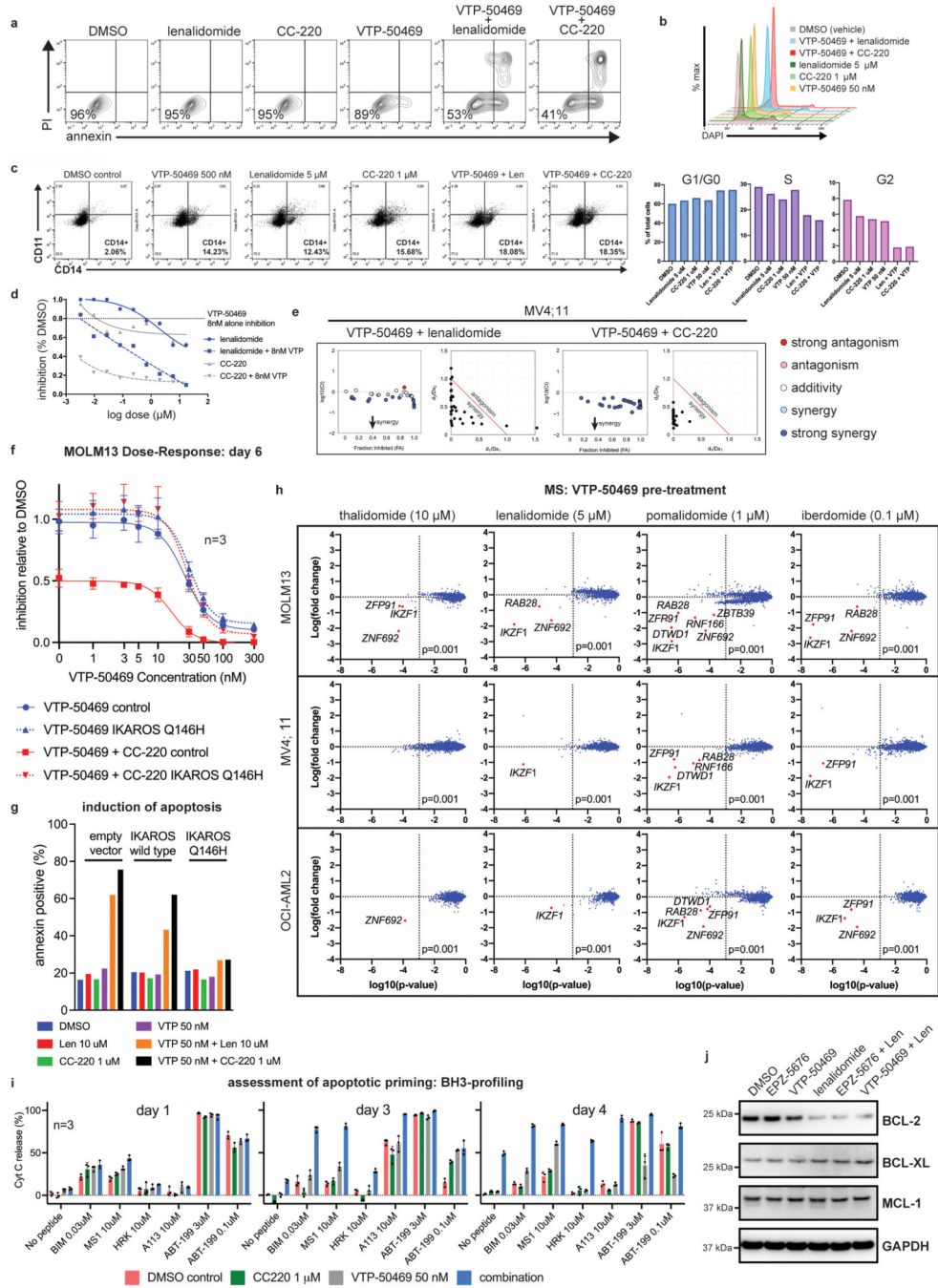
GSEA computational method. **e**, Bar code plots created using the GSEA tool for putative MLL-fusion target genes with selected genes from leading edge analysis indicated with $\text{adj-p-value} < 0.05$ in MOLM13 or MV4;11. Normalized enrichment score and family-wise error rate p-value as determined by GSEA computational method. **f**, Gene expression z-score heatmap for selected genes within immune regulatory and inflammatory pathways under treatment with CC220 (n=3) compared to DMSO-treated control (n=3). **g**, Venn diagram for genes displaying > 2-fold change in expression following CC-220 treatment comparing cell lines. Gene number and percentage overlap is indicated. Selected genes deregulated in both cell lines are indicated. **h**, Correlation of IKAROS-bound gene TSSes, determined by ChIP-seq, with RNA-seq changes. Bar code plot showing gene expression changes following treatment with CC220 (3 days) for the top 500 genes bound by IKAROS (by peak enrichment over background). Selected genes from leading edge analysis indicated. Normalized enrichment score and family-wise error rate p-value determined by GSEA computational method. **i**, Correlation of IKAROS-bound enhancers, determined by ChIP-seq and the ABC prediction tool, with RNA-seq gene expression changes. Bar code plots display gene expression changes following treatment with CC-220 (3 days) for the top 500 genes predicted to be regulated by IKAROS-bound enhancers (by peak enrichment over background at enhancers). Normalized enrichment score and family-wise error rate p-value determined by GSEA computational method. Venn diagram for overlap between gene expression change and genes predicted to be regulated by the top 1000 IKAROS-bound enhancers.



Extended Data Fig. 5. IKAROS CUT&RUN motif foot printing.

a, *IKZF1* DNA-binding motifs. **b**, Foot printing for CTCF protein over the *CTCF* motif for each cell line; used as a positive control for motif detection. Result for CUT&RUNTools *de novo* DREME motif detection is shown with highly significant discovery of the known *CTCF* motif. MEME and E-value is indicated. **c**, CUT&RUNTools foot printing for IKAROS and IgG control over the *IKZF1* motif in the MOLM13 cell line. Cut site probability distribution as determined by CUT&RUNTools. **d**, CUT&RUNTools foot printing for IKAROS over the JUN:FOS motif (centrally bound), CEBPα motif (centrally

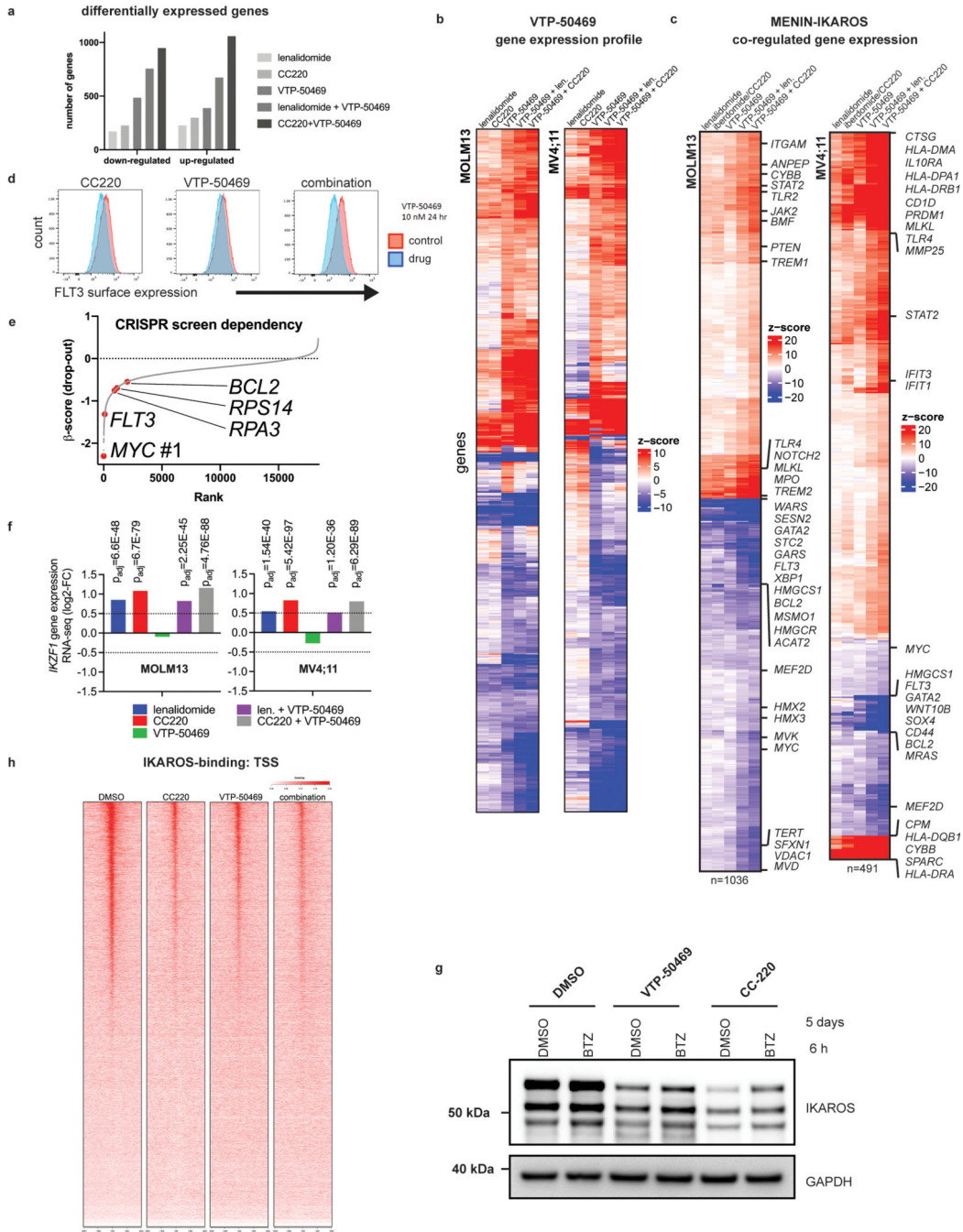
bound), SPI/Pu.1 motif (centrally bound) and the RUNX motif (non-centrally bound), as indicated, in the MOLM13 cell line. Cut site probability distribution as determined by CUT&RUNTools.



Extended Data Fig. 6. Combined targeting of MENIN and IKAROS.

a, Annexin V staining (apoptosis) by flow cytometry following 6 days treatment with VTP-50469, LEN, CC220 and combination (MOLM13). **b**, Cell cycle analysis: histogram for DAPI stain and bar graphs displaying cell cycle stage (%) are shown for each condition.

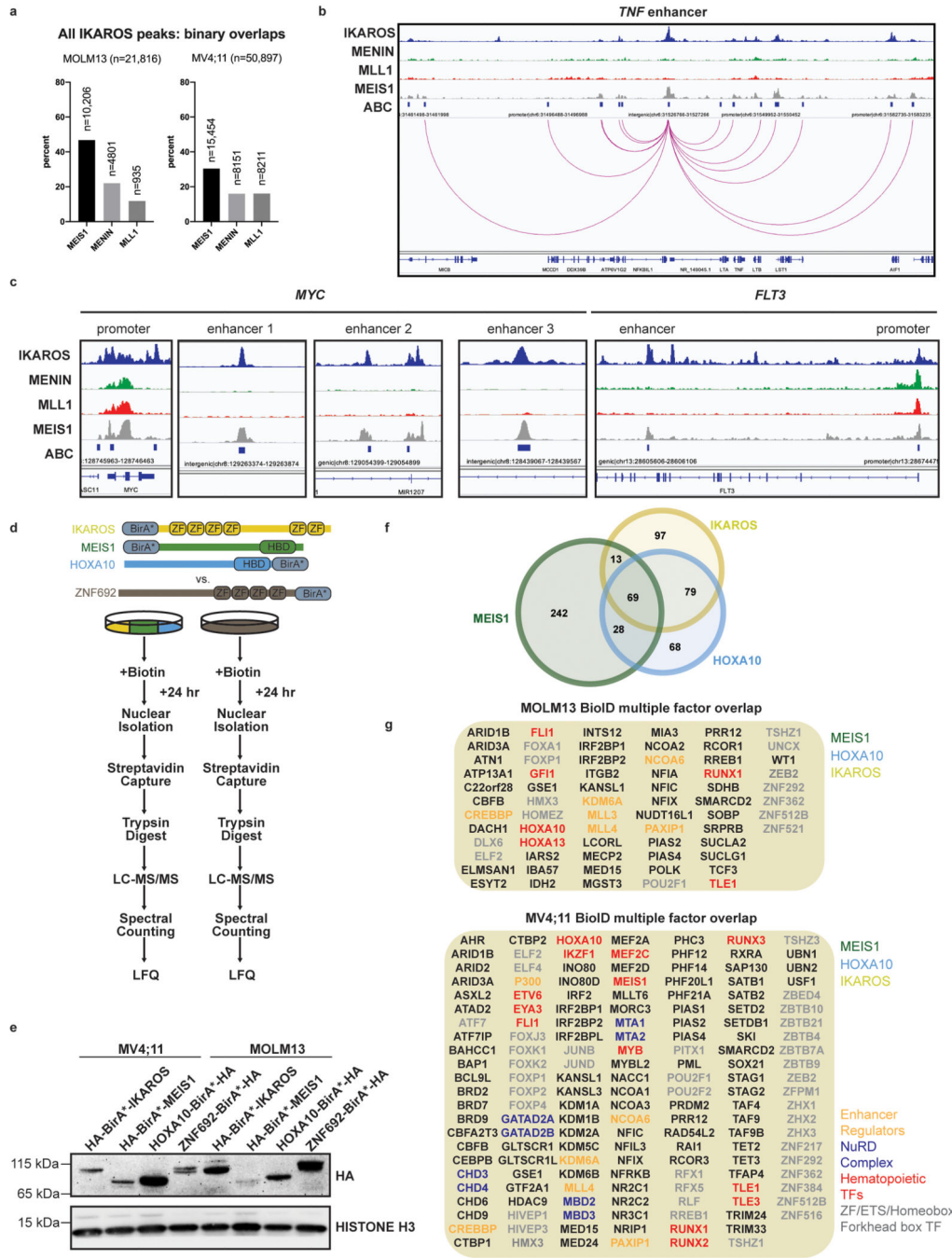
Representative experiment shown. (MOLM13) **c**, CD11b/CD14 expression measured by flow cytometry 6 days following treatment with VTP-50469, LEN, CC220 and combination (MOLM13). Representative experiment shown. **d**, Dose-response curves for LEN and CC220, with and without VTP-50469 (8 nM), compared to VTP-50469 alone (dotted line) measured by Cell-Titer Glo in MV4;11 for synergy studies. **e**, Chou-Talalay synergy analysis for VTP-50469 in combination with LEN or CC-220 (MV4;11). Chou-Talalay Combination Index (CI) plots (left panel) and normalized isobolograms (right panel) are shown for each IMiD-VTP-50469 combination (day 6). Line of additivity is shown (red). **f**, CC-220 and MENIN inhibitor dose response curves (day 6) with and without overexpression of non-degradable IKAROS (Q146H) in MOLM13. Data represent mean+/-SD with non-linear regression curve fit shown. **g**, IMiD and MENIN inhibitor apoptosis after 6 days treatment, with and without overexpression of a wild-type IKAROS or non-degradable IKAROS mutant (Q146H) in MOLM13. **h**, Scatterplots for mass spectrometry (MS) results on MOLM13, MV4;11 and OCI-AML2 cell lines after 5 days pre-treatment with VTP-50469 and then treatment with THAL, LEN, POM and CC-220 (iberdomide), for 5 h. Data represent the log-fold change in abundance and log₁₀(p-value). p-value determined by moderated t-test as implemented by the Bioconductor Limma package. **i**, BH3-profiling in MV4;11 under drug treatments indicated. Cytochrome C (Cyt C) release was measured. Data represent mean+/-SEM (n=3). **j**, Western blot analysis for BCL2, MCL1 and BCL-XL protein following treatment of OCI-AML2 human *MLL-r* AML cell line for 72 hours with LEN, EPZ-5676, VTP-50469 and each combination, using GAPDH as a loading control.



Extended Data Fig. 7. MENIN and IKAROS display overlapping functions in regulation of gene expression.

a. Number of differentially expressed genes (greater than 2-fold change and adjusted p-value <0.05) from RNA-seq data for MOLM13 and MV4;11 cell lines treated with CC220 1 μ M (n=3), VTP-50469 50 nM (n=3) and the combination (n=3) for 3 days. **b.** Heatmap showing DESeq2 statistical z-score for all genes deregulated under treatment with VTP-50469 alone across all other treatment groups. **c.** Heatmap of DESeq2 statistical z-score for MENIN and IKAROS co-regulated gene expression. Showing genes with shared or additive regulation.

Selected genes are indicated. **d**, Cell surface expression of FLT3 as measured by flow cytometry in the MOLM13 cell line. Cells were pre-treated for 2 days with CC220 or DMSO control and then VTP-50469 was added for 24 hours. **e**, CRISPR screen beta scores from MAGeCK MLE comparing *sgRNA* representation at day 0 compared to day 14 in the DMSO-treated control samples for the MOLM13 cell line. Negative beta scores for *MYC*, *FLT3*, *RPA3* (common essential gene), *RPS14*, and *BCL2* are indicated. **f**, Gene expression for *IKZF1* as determined by RNA-seq in MOLM13 and MV4;11, indicating log-2-fold change value and adjusted p-value determined using DESeq2. **g**, Western blot analysis for IKAROS protein in the MOLM13 cell line following 5 days treatment with either VTP-50469 or iberdomide/CC220, followed by rescue treatment with bortezomib (BTZ) for 6 hours, using GAPDH as a loading control. Performed in the presence of the broad-spectrum caspase inhibitor, QV-D-OPH, to prevent cell death. **h**, Tornado plots depicting global IKAROS chromatin binding at TSSes, as determined by CUT&RUN in the MOLM13 cell line.



Extended Data Fig. 8. IKAROS protein interactome in MLL-r AML.

a, Binary overlap percentage between all IKAROS peaks enriched 5-fold over background, genome-wide, with each of the other 3 factors, MEIS1 (at 15FE), MENIN (at 5FE) and MLL1 (at 5FE) according ChIP-seq data. **b**, IGV tracks depicting binding of IKAROS, MENIN, MLL1 and MEIS1, as determined by ChIP-seq, in the region of the TNF gene. Promoters and enhancers, predicted from the ABC tool, are indicated with genomic location indicated (Hg19). **c**, IGV tracks depicting binding of IKAROS, MENIN, MLL1 and MEIS1 at the MYC and FLT3 genes as determined by ChIP-seq. Promoters and selected enhancers,

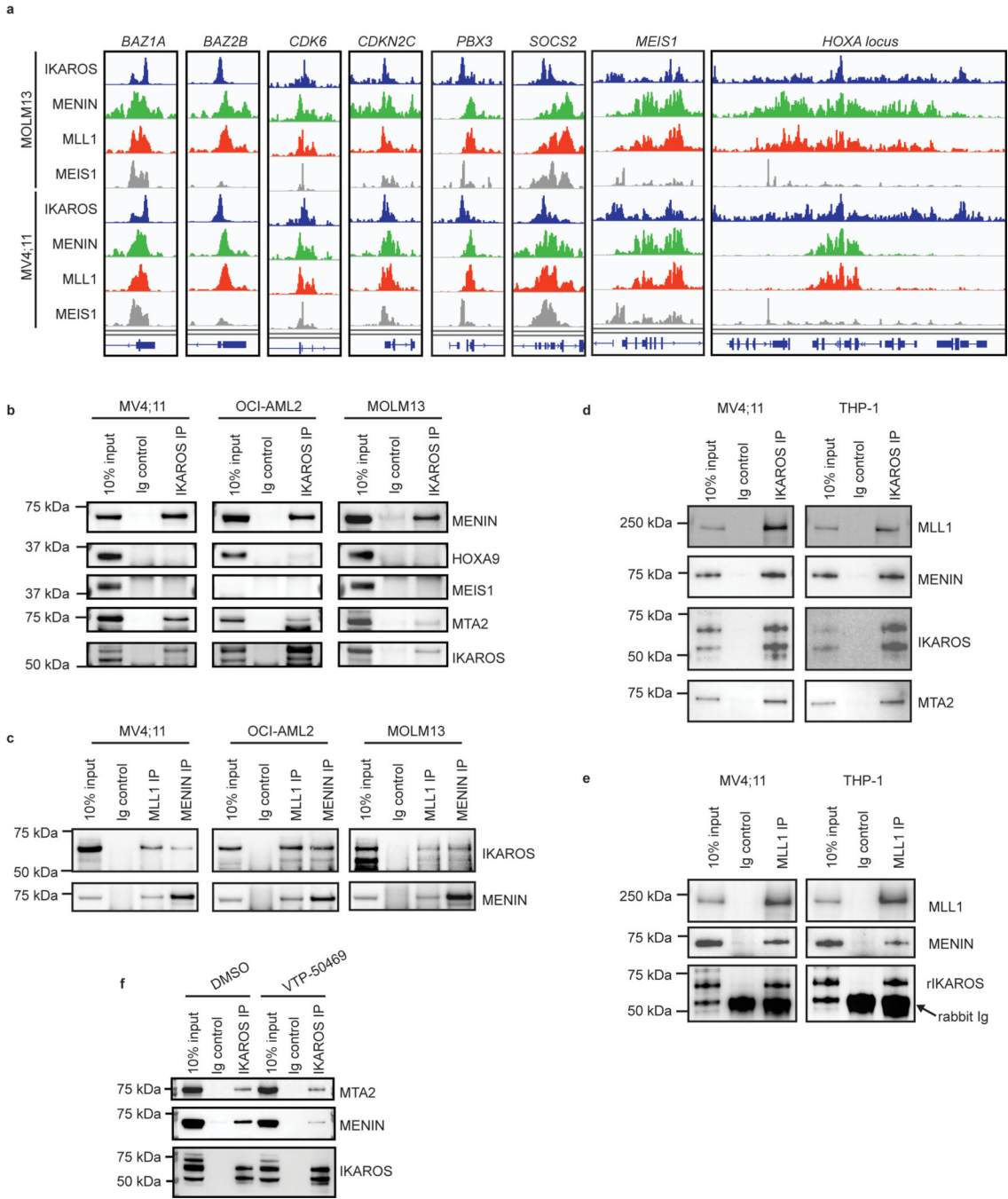
predicted from the ABC tool, are indicated with genomic location indicated (Hg19). **d**, Schematic diagrams of protein domains and experimental workflow of BioID system. IKAROS, MEIS1, HOXA10 and ZNF692 proteins were tagged with the biotin ligase BirA*, the left side of the protein schematic diagram denotes N-terminal tagging and the right-side, C-terminal. MV4;11 and MOLM13 cells expressing BioID constructs, 8 total cell lines, were cultured separately. ZF=Zinc finger domain, HBD=homeobox domain, LFQ=label free quantitation, LC-MS/MS=liquid chromatography coupled tandem mass spectrometry. **e**, Western Blot analysis of the expression of BirA* and HA tagged fusion proteins in MV4;11 and MOLM13 cells, using total Histone H3 as a loading control. **f**, Venn diagram displaying the number of proteins identified in label free quantitation analysis of the MOLM13 IKAROS, MEIS1 and HOXA10 BioID LC-MS/MS data. All proteins included in Venn diagram have a >2-fold enrichment over the ZNF692 control. **g**, List of proteins common to IKAROS, MEIS1, HOXA10 BioID identified in LFQ analysis having >2-fold enrichment over the ZNF692 control in the MV4;11 and MOLM13 cell lines.

Author Manuscript

Author Manuscript

Author Manuscript

Author Manuscript



Extended Data Fig. 9. IKAROS and MENIN co-reside within an isolatable protein complex.

a, IGV ChIP-seq tracks for IKAROS, MENIN, MEIS1 and MLL1 at selected gene TSSes. Tracks are derived from the same ChIP-seq experiments depicted in Fig. 6 and Extended Data Fig. 8. **b**, Direct protein Co-IP using IKAROS as the bait and probed for MENIN, HOXA9, MEIS1, MTA2 and IKAROS in the MV4;11, OCI-AML2 and MOLM13 cell lines using high salt nuclear extraction and detergent wash. **c**, Direct protein Co-IP using MLL1 and MENIN as the bait and probed for MENIN and IKAROS, in the MV4;11, OCI-AML2 and MOLM13 cell lines using high salt nuclear extraction and detergent wash. **d**, Direct

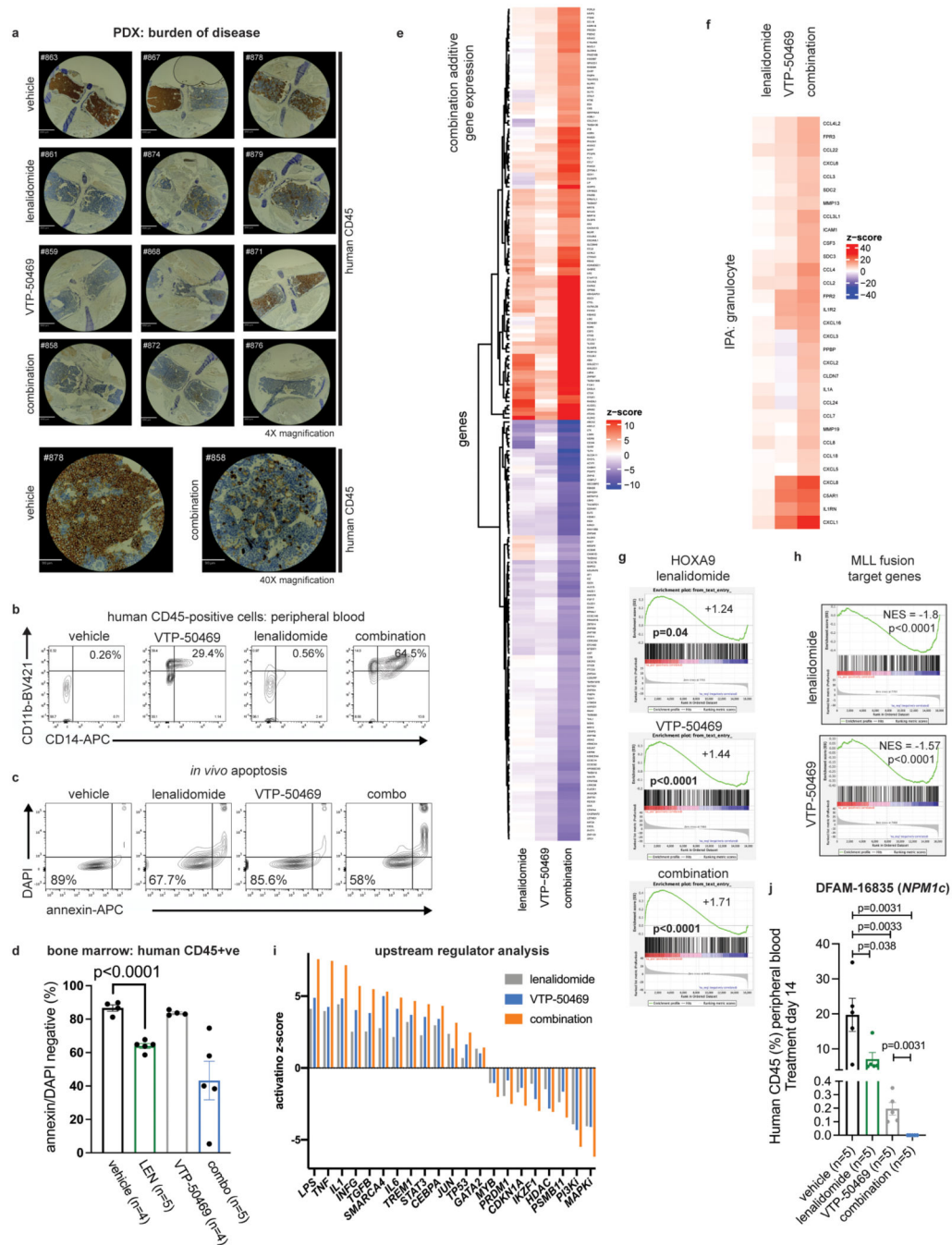
protein Co-IP using IKAROS as the bait and probed for MENIN, MLL1, IKAROS and MTA2 in the MV4;11 and THP-1 cell lines using benzonase-treated nuclear extract and high glycerol wash. **e**, Direct protein Co-IP using MLL1 (rabbit antibody) and MENIN (rabbit antibody) as the bait and probed for MLL1, MENIN and rabbit IKAROS antibody (rIKAROS), in the MV4;11 and THP-1 cell lines using benzonase-treated nuclear extract and high glycerol wash. Rabbit immunoglobulin is seen overlying the IKAROS Western blot bands (indicated in the figure) due to the use of an anti-rabbit secondary antibody. **f**, Direct protein Co-IP using IKAROS as the bait, with and without prior VTP-50469 treatment (250 nM for 48 hr), and probed for MENIN, MTA2, and IKAROS, in the THP-1 cell line.

Author Manuscript

Author Manuscript

Author Manuscript

Author Manuscript



Extended Data Fig. 10. Combination therapy with VTP-50469 and LEN results in additive anti-leukemic activity *in vivo*.

a, Immunohistochemistry for human CD45 antigen on bone marrow sections (sternum) on PDX/CBAM-68552 following 3 weeks treatment with vehicle, LEN 50 mg/kg daily, VTP-50469 0.1% rodent diet and the drug combination. **b**, Analysis of differentiation in circulating leukaemia cells using CD11b and CD14 expression assessed by flow cytometry in CBAM-68552 after 3 weeks drug treatment. Percentage of double-positive cells is indicated. Representative examples from individual mice are shown. **c**, Assessment of

apoptosis in human CD45-positive cells from bone marrow of drug-treated mice using the CBSK-17D model following 2 weeks drug treatment. The percentage of total viable, human cells are indicated. Representative examples from individual mice are shown. **d**, Quantitation of apoptotic cells from bone marrow of mice transplanted with the CBSK-17D PDX model following 2 weeks drug treatment. Data represent mean \pm SEM with p-value by unpaired two-tail t-test. **e**, RNA-seq heatmap from PDX/CBAM-68552 following 3 weeks treatment with vehicle, LEN 50 mg/kg daily, VTP-50469 0.1% rodent diet and the drug combination. Heatmap displaying RNA-Seq DESeq2 statistical z-score for the co-regulated gene network between VTP-50469 and LEN **f**, RNA-seq heatmap displaying DESeq2 statistical z-score for genes detected in the “granulocyte” pathway as additively deregulated using QIAGEN Ingenuity Pathway Analysis (IPA) analysis. **g**, Bar code plots using the gene set for HOXA9 regulated genes under each drug treatment from RNA-seq *in vivo* using the PDX/CBAM-68552 model. Normalized enrichment score and family-wise error rate p-value determined by the GSEA computational method. **h**, Gene set testing for reported MLL-fusion gene targets for LEN and VTP-50469. Family-wise p-value and normalized enrichment score (NES) determined by the GSEA computational method. **i**, IPA upstream regulator analysis. Graph displays selected activation z-scores for detected pathways with p-value <0.05. **j**, Measurement of peripheral blood circulating human CD45 positive cells from PDX mice transplanted with the DFAM-16835 PDX model (*NPM1c*) after two weeks of drug treatment *in vivo*. Data represent mean \pm SEM with p-value determined using unpaired, two-tail t-test.

Supplementary Material

Refer to Web version on PubMed Central for supplementary material.

Acknowledgements

S.A.A. is supported by NIH grants CA176745, CA206963, CA204639 and CA066996 and by the Leukaemia and Lymphoma Society, USA (LLS). B.J.A. receives a Career Development Fellowship from the LLS. J.A.C. is supported by Ruth L. Kirschstein Postdoctoral Individual National Research Service Award (NIH F32CA250240-02). W.B. is supported by an NIH T32 training grant (5T32HL007574-38) and the Wong Family Award in Translational Oncology. S.G. is supported by the Sara Elizabeth O'Brien Trust Fellowship. X.S.L. is supported by the Breast Cancer Research Foundation (BCRF-20-100). E.S.F. is supported by NIH grants CA214608, CA231637 and CA066996 and by a Damon Runyon-Rachleff Innovator Award DRR-50-18. S.N.O. is supported by the Damon Runyon Cancer Research Foundation (DRSG: 26-18). F.P. is supported by a grant from the German Research Foundation (PE 3217/1-1). A.C. received funding by German Cancer Aid (Deutsche Krebshilfe). We are grateful for support from the St. Baldrick's Foundation to the Pediatric LEAP Consortium. We thank all members of the Armstrong lab for invaluable discussions. We thank Jennifer Perry, Yana Pikman, and Andrea Pinilla along with the CPCT for the development and use of human PDX models. We are extremely grateful to Andrea Pinilla, Amy Conway, Amanda Robichaud, Prafulla Gokhale and the Experimental Therapeutics Core Facility at Dana-Farber Cancer Institute for assistance with mouse studies. We thank James Healey, Jayant Gadrey and Sayuri Kitajima for technical support. We thank Elizabeth Frank and Kenneth Ross for statistical analyses. We thank Emma Fink, Andrew Guirguis, Quinlan Sievers, and Vidyasagar Koduri for advice on IKAROS studies and *in vivo* studies. We thank Martin Filipovski for invaluable assistance with CUT&RUN experiments. The content is solely the responsibility of the authors and does not represent the official views of the National Institutes of Health.

Declaration of Competing Interests

S.A.A. has been a consultant and/or shareholder for Neomorph Inc, Imago Biosciences, Vitae/Allergan Pharma, Cyteir Therapeutics, C4 Therapeutics, OxStem Oncology, Accent Therapeutics, and Mana Therapeutics. S.A.A. has received research support from Janssen, Novartis, Syndax, and AstraZeneca. X.S.L. is a cofounder, board member, SAB, and consultant of GV20 Oncotherapy and its subsidiaries, SAB of 3DMedCare, consultant for Genentech, and stockholder of ABT, AMGN, JNJ, MRK, PFE, and receives sponsored research funding from Takeda and

Sanofi. G.M.McG. is a shareholder of Syndax Pharmaceuticals. B.J.A. is a former employee of the Walter and Eliza Hall Institute of Medical Research, Melbourne, Australia, and receives proceeds from Royalties and Milestone payments related to the BCL2-inhibitor, ABT-199/venetoclax. E.S.F. is an equity holder and scientific advisor for Civetta therapeutics, Jengu therapeutics (board of directors), and Neomorph Inc, a shareholder in C4 Therapeutics and a consultant to EcoR1 Capital, Sanofi, Astellas, Deerfield and RA Capital. The Fischer lab receives or has received research funding from Novartis, Astellas, Deerfield, and Ajax. All other authors declare no potential conflicts of interest.

References

1. Valk PJ et al. Prognostically useful gene-expression profiles in acute myeloid leukemia. *N Engl J Med* 350, 1617–1628, doi:10.1056/NEJMoa040465 (2004). [PubMed: 15084694]
2. Bullinger L. et al. Use of gene-expression profiling to identify prognostic subclasses in adult acute myeloid leukemia. *N Engl J Med* 350, 1605–1616, doi:10.1056/NEJMoa031046 (2004). [PubMed: 15084693]
3. Krivtsov AV, Hoshii T. & Armstrong SA Mixed-Lineage Leukemia Fusions and Chromatin in Leukemia. *Cold Spring Harb Perspect Med* 7, doi:10.1101/cshperspect.a026658 (2017).
4. Novershtern N. et al. Densely interconnected transcriptional circuits control cell states in human hematopoiesis. *Cell* 144, 296–309, doi:10.1016/j.cell.2011.01.004 (2011). [PubMed: 21241896]
5. Yokoyama A. et al. The menin tumor suppressor protein is an essential oncogenic cofactor for MLL-associated leukemogenesis. *Cell* 123, 207–218, doi:10.1016/j.cell.2005.09.025 (2005). [PubMed: 16239140]
6. Yokoyama A. & Cleary ML Menin critically links MLL proteins with LEDGF on cancer-associated target genes. *Cancer Cell* 14, 36–46, doi:10.1016/j.ccr.2008.05.003 (2008). [PubMed: 18598942]
7. Okada Y. et al. hDOT1L links histone methylation to leukemogenesis. *Cell* 121, 167–178, doi:10.1016/j.cell.2005.02.020 (2005). [PubMed: 15851025]
8. Bernt KM et al. MLL-rearranged leukemia is dependent on aberrant H3K79 methylation by DOT1L. *Cancer Cell* 20, 66–78, doi:10.1016/j.ccr.2011.06.010 (2011). [PubMed: 21741597]
9. Smith E, Lin C. & Shilatfard A. The super elongation complex (SEC) and MLL in development and disease. *Genes Dev* 25, 661–672, doi:10.1101/gad.2015411 (2011). [PubMed: 21460034]
10. Brown FC et al. MEF2C Phosphorylation Is Required for Chemotherapy Resistance in Acute Myeloid Leukemia. *Cancer Discov* 8, 478–497, doi:10.1158/2159-8290.CD-17-1271 (2018). [PubMed: 29431698]
11. Krivtsov AV et al. Transformation from committed progenitor to leukaemia stem cell initiated by MLL-AF9. *Nature* 442, 818–822, doi:10.1038/nature04980 (2006). [PubMed: 16862118]
12. Placke T. et al. Requirement for CDK6 in MLL-rearranged acute myeloid leukemia. *Blood* 124, 13–23, doi:10.1182/blood-2014-02-558114 (2014). [PubMed: 24764564]
13. Faber J. et al. HOXA9 is required for survival in human MLL-rearranged acute leukemias. *Blood* 113, 2375–2385, doi:10.1182/blood-2007-09-113597 (2009). [PubMed: 19056693]
14. Guo H. et al. PBX3 is essential for leukemia stem cell maintenance in MLL-rearranged leukemia. *Int J Cancer* 141, 324–335, doi:10.1002/ijc.30739 (2017). [PubMed: 28411381]
15. Kumar AR et al. A role for MEIS1 in MLL-fusion gene leukemia. *Blood* 113, 1756–1758, doi:10.1182/blood-2008-06-163287 (2009). [PubMed: 19109563]
16. Collins C. et al. C/EBPalpha is an essential collaborator in Hoxa9/Meis1-mediated leukemogenesis. *Proc Natl Acad Sci U S A* 111, 9899–9904, doi:10.1073/pnas.1402238111 (2014). [PubMed: 24958854]
17. Wilkinson AC et al. RUNX1 is a key target in t(4;11) leukemias that contributes to gene activation through an AF4-MLL complex interaction. *Cell Rep* 3, 116–127, doi:10.1016/j.celrep.2012.12.016 (2013). [PubMed: 23352661]
18. Sun Y. et al. HOXA9 Reprograms the Enhancer Landscape to Promote Leukemogenesis. *Cancer Cell* 34, 643–658 e645, doi:10.1016/j.ccell.2018.08.018 (2018). [PubMed: 30270123]
19. Cusan M. et al. LSD1 inhibition exerts its antileukemic effect by recommissioning PU.1- and C/EBPalpha-dependent enhancers in AML. *Blood* 131, 1730–1742, doi:10.1182/blood-2017-09-807024 (2018). [PubMed: 29453291]

20. Zhu N. et al. MLL-AF9- and HOXA9-mediated acute myeloid leukemia stem cell self-renewal requires JMJD1C. *J Clin Invest* 126, 997–1011, doi:10.1172/JCI82978 (2016). [PubMed: 26878175]
21. Zeisig BB et al. Hoxa9 and Meis1 are key targets for MLL-ENL-mediated cellular immortalization. *Mol Cell Biol* 24, 617–628, doi:10.1128/mcb.24.2.617-628.2004 (2004). [PubMed: 14701735]
22. Kuhn MW et al. Targeting Chromatin Regulators Inhibits Leukemogenic Gene Expression in NPM1 Mutant Leukemia. *Cancer Discov* 6, 1166–1181, doi:10.1158/2159-8290.CD-16-0237 (2016). [PubMed: 27535106]
23. Bradner JE, Hnisz D. & Young RA Transcriptional Addiction in Cancer. *Cell* 168, 629–643, doi:10.1016/j.cell.2016.12.013 (2017). [PubMed: 28187285]
24. Krivtsov AV et al. A Menin-MLL Inhibitor Induces Specific Chromatin Changes and Eradicates Disease in Models of MLL-Rearranged Leukemia. *Cancer Cell* 36, 660–673 e611, doi:10.1016/j.ccell.2019.11.001 (2019). [PubMed: 31821784]
25. Borkin D. et al. Pharmacologic inhibition of the Menin-MLL interaction blocks progression of MLL leukemia in vivo. *Cancer Cell* 27, 589–602, doi:10.1016/j.ccell.2015.02.016 (2015). [PubMed: 25817203]
26. Klossowski S. et al. Menin inhibitor MI-3454 induces remission in MLL1-rearranged and NPM1-mutated models of leukemia. *J Clin Invest* 130, 981–997, doi:10.1172/JCI129126 (2020). [PubMed: 31855575]
27. Daigle SR et al. Potent inhibition of DOT1L as treatment of MLL-fusion leukemia. *Blood* 122, 1017–1025, doi:10.1182/blood-2013-04-497644 (2013). [PubMed: 23801631]
28. Perner F. et al. Novel inhibitors of the histone methyltransferase DOT1L show potent antileukemic activity in patient-derived xenografts. *Blood* 136, 1983–1988, doi:10.1182/blood.2020006113 (2020). [PubMed: 32575123]
29. Uckelmann HJ et al. Therapeutic targeting of preleukemia cells in a mouse model of NPM1 mutant acute myeloid leukemia. *Science* 367, 586–590, doi:10.1126/science.aax5863 (2020). [PubMed: 32001657]
30. Stein EM et al. The DOT1L inhibitor pinometostat reduces H3K79 methylation and has modest clinical activity in adult acute leukemia. *Blood* 131, 2661–2669, doi:10.1182/blood-2017-12-818948 (2018). [PubMed: 29724899]
31. Perner F. & Armstrong SA Targeting Chromatin Complexes in Myeloid Malignancies and Beyond: From Basic Mechanisms to Clinical Innovation. *Cells* 9, doi:10.3390/cells9122721 (2020).
32. Wang B. et al. Integrative analysis of pooled CRISPR genetic screens using MAGeCKFlute. *Nat Protoc* 14, 756–780, doi:10.1038/s41596-018-0113-7 (2019). [PubMed: 30710114]
33. Lai AY & Wade PA Cancer biology and NuRD: a multifaceted chromatin remodelling complex. *Nat Rev Cancer* 11, 588–596, doi:10.1038/nrc3091 (2011). [PubMed: 21734722]
34. Cerami E. et al. The cBio cancer genomics portal: an open platform for exploring multidimensional cancer genomics data. *Cancer Discov* 2, 401–404, doi:10.1158/2159-8290.CD-12-0095 (2012). [PubMed: 22588877]
35. Meyers RM et al. Computational correction of copy number effect improves specificity of CRISPR-Cas9 essentiality screens in cancer cells. *Nat Genet* 49, 1779–1784, doi:10.1038/ng.3984 (2017). [PubMed: 29083409]
36. Brunetti L. et al. Mutant NPM1 Maintains the Leukemic State through HOX Expression. *Cancer Cell* 34, 499–512 e499, doi:10.1016/j.ccell.2018.08.005 (2018). [PubMed: 30205049]
37. Kronke J. et al. Lenalidomide causes selective degradation of IKZF1 and IKZF3 in multiple myeloma cells. *Science* 343, 301–305, doi:10.1126/science.1244851 (2014). [PubMed: 24292625]
38. Lu G. et al. The myeloma drug lenalidomide promotes the cereblon-dependent destruction of Ikaros proteins. *Science* 343, 305–309, doi:10.1126/science.1244917 (2014). [PubMed: 24292623]
39. Kronke J. et al. Lenalidomide induces ubiquitination and degradation of CK1alpha in del(5q) MDS. *Nature* 523, 183–188, doi:10.1038/nature14610 (2015). [PubMed: 26131937]
40. Donovan KA et al. Thalidomide promotes degradation of SALL4, a transcription factor implicated in Duane Radial Ray syndrome. *Elife* 7, doi:10.7554/eLife.38430 (2018).

41. Guenther MG et al. Aberrant chromatin at genes encoding stem cell regulators in human mixed-lineage leukemia. *Genes Dev* 22, 3403–3408, doi:10.1101/gad.1741408 (2008). [PubMed: 19141473]
42. Skene PJ & Henikoff S. An efficient targeted nuclease strategy for high-resolution mapping of DNA binding sites. *Elife* 6, doi:10.7554/eLife.21856 (2017).
43. Meers MP, Bryson TD, Henikoff JG & Henikoff S. Improved CUT&RUN chromatin profiling tools. *Elife* 8, doi:10.7554/eLife.46314 (2019).
44. Zhu Q, Liu N, Orkin SH & Yuan GC CUT&RUNTools: a flexible pipeline for CUT&RUN processing and footprint analysis. *Genome Biol* 20, 192, doi:10.1186/s13059-019-1802-4 (2019). [PubMed: 31500663]
45. Fulco CP et al. Activity-by-contact model of enhancer-promoter regulation from thousands of CRISPR perturbations. *Nat Genet* 51, 1664–1669, doi:10.1038/s41588-019-0538-0 (2019). [PubMed: 31784727]
46. Ryan JA, Brunelle JK & Letai A. Heightened mitochondrial priming is the basis for apoptotic hypersensitivity of CD4⁺ CD8⁺ thymocytes. *Proc Natl Acad Sci U S A* 107, 12895–12900, doi:10.1073/pnas.0914878107 (2010). [PubMed: 20615979]
47. Samavarchi-Tehrani P, Samson R. & Gingras AC Proximity Dependent Biotinylation: Key Enzymes and Adaptation to Proteomics Approaches. *Mol Cell Proteomics* 19, 757–773, doi:10.1074/mcp.R120.001941 (2020). [PubMed: 32127388]
48. Guirguis AA & Ebert BL Lenalidomide: deciphering mechanisms of action in myeloma, myelodysplastic syndrome and beyond. *Curr Opin Cell Biol* 37, 61–67, doi:10.1016/j.jceb.2015.10.004 (2015). [PubMed: 26512454]
49. Fink EC et al. Crbn (I391V) is sufficient to confer in vivo sensitivity to thalidomide and its derivatives in mice. *Blood* 132, 1535–1544, doi:10.1182/blood-2018-05-852798 (2018). [PubMed: 30064974]
50. Francis OL, Payne JL, Su RJ & Payne KJ Regulator of myeloid differentiation and function: The secret life of Ikaros. *World J Biol Chem* 2, 119–125, doi:10.4331/wjbc.v2.i6.119 (2011). [PubMed: 21765977]
51. Boutboul D. et al. Dominant-negative IKZF1 mutations cause a T, B, and myeloid cell combined immunodeficiency. *J Clin Invest* 128, 3071–3087, doi:10.1172/JCI98164 (2018). [PubMed: 29889099]
52. Yoshida T, Ng SY, Zuniga-Pflucker JC & Georgopoulos K. Early hematopoietic lineage restrictions directed by Ikaros. *Nat Immunol* 7, 382–391, doi:10.1038/ni1314 (2006). [PubMed: 16518393]
53. Martinez-Hoyer S. et al. Loss of lenalidomide-induced megakaryocytic differentiation leads to therapy resistance in del(5q) myelodysplastic syndrome. *Nat Cell Biol* 22, 526–533, doi:10.1038/s41556-020-0497-9 (2020). [PubMed: 32251398]
54. Georgopoulos K. Haematopoietic cell-fate decisions, chromatin regulation and ikaros. *Nat Rev Immunol* 2, 162–174, doi:10.1038/nri747 (2002). [PubMed: 11913067]
55. Bottardi S, Mavoungou L. & Milot E. IKAROS: a multifunctional regulator of the polymerase II transcription cycle. *Trends Genet* 31, 500–508, doi:10.1016/j.tig.2015.05.003 (2015). [PubMed: 26049627]
56. Ding Y. et al. Ikaros tumor suppressor function includes induction of active enhancers and super-enhancers along with pioneering activity. *Leukemia* 33, 2720–2731, doi:10.1038/s41375-019-0474-0 (2019). [PubMed: 31073152]
57. Scacheri PC et al. Genome-wide analysis of menin binding provides insights into MEN1 tumorigenesis. *PLoS Genet* 2, e51, doi:10.1371/journal.pgen.0020051 (2006). [PubMed: 16604156]
58. Skucha A. et al. MLL-fusion-driven leukemia requires SETD2 to safeguard genomic integrity. *Nat Commun* 9, 1983, doi:10.1038/s41467-018-04329-y (2018). [PubMed: 29777171]
59. Hughes CM et al. Menin associates with a trithorax family histone methyltransferase complex and with the hoxc8 locus. *Mol Cell* 13, 587–597, doi:10.1016/s1097-2765(04)00081-4 (2004). [PubMed: 14992727]

60. Bres V, Yoshida T, Pickle L. & Jones KA SKIP interacts with c-Myc and Menin to promote HIV-1 Tat transactivation. *Mol Cell* 36, 75–87, doi:10.1016/j.molcel.2009.08.015 (2009). [PubMed: 19818711]
61. Agarwal SK et al. Menin interacts with the AP1 transcription factor JunD and represses JunD-activated transcription. *Cell* 96, 143–152, doi:10.1016/s0092-8674(00)80967-8 (1999). [PubMed: 9989505]
62. Huang J. et al. The same pocket in menin binds both MLL and JUND but has opposite effects on transcription. *Nature* 482, 542–546, doi:10.1038/nature10806 (2012). [PubMed: 22327296]
63. Wu Y. et al. Disruption of the menin-MLL interaction triggers menin protein degradation via ubiquitin-proteasome pathway. *Am J Cancer Res* 9, 1682–1694 (2019). [PubMed: 31497350]
64. Xie CH et al. Efficacy and safety of lenalidomide for the treatment of acute myeloid leukemia: a systematic review and meta-analysis. *Cancer Manag Res* 10, 3637–3648, doi:10.2147/CMAR.S168610 (2018). [PubMed: 30271212]
65. Ebert BL & Kronke J. Inhibition of Casein Kinase 1 Alpha in Acute Myeloid Leukemia. *N Engl J Med* 379, 1873–1874, doi:10.1056/NEJMcibr1811318 (2018). [PubMed: 30403945]
66. Le Roy A. et al. Immunomodulatory Drugs Exert Anti-Leukemia Effects in Acute Myeloid Leukemia by Direct and Immunostimulatory Activities. *Front Immunol* 9, 977, doi:10.3389/fimmu.2018.00977 (2018). [PubMed: 29780393]
67. Fang J. et al. A calcium- and calpain-dependent pathway determines the response to lenalidomide in myelodysplastic syndromes. *Nat Med* 22, 727–734, doi:10.1038/nm.4127 (2016). [PubMed: 27294874]

Online-only References

68. Kluk MJ et al. Validation and Implementation of a Custom Next-Generation Sequencing Clinical Assay for Hematologic Malignancies. *J Mol Diagn* 18, 507–515, doi:10.1016/j.jmoldx.2016.02.003 (2016). [PubMed: 27339098]
69. Townsend EC et al. The Public Repository of Xenografts Enables Discovery and Randomized Phase II-like Trials in Mice. *Cancer Cell* 29, 574–586, doi:10.1016/j.ccell.2016.03.008 (2016). [PubMed: 27070704]
70. Chi HT et al. Detection of exon 12 type A mutation of NPM1 gene in IMS-M2 cell line. *Leuk Res* 34, 261–262, doi:10.1016/j.leukres.2009.09.019 (2010). [PubMed: 19854508]
71. Fei T. et al. Deciphering essential cistromes using genome-wide CRISPR screens. *Proc Natl Acad Sci U S A* 116, 25186–25195, doi:10.1073/pnas.1908155116 (2019). [PubMed: 31727847]
72. Li W. et al. MAGeCK enables robust identification of essential genes from genome-scale CRISPR/Cas9 knockout screens. *Genome Biol* 15, 554, doi:10.1186/s13059-014-0554-4 (2014). [PubMed: 25476604]
73. Doench JG et al. Rational design of highly active sgRNAs for CRISPR-Cas9-mediated gene inactivation. *Nat Biotechnol* 32, 1262–1267, doi:10.1038/nbt.3026 (2014). [PubMed: 25184501]
74. Dignam JD, Lebovitz RM & Roeder RG Accurate transcription initiation by RNA polymerase II in a soluble extract from isolated mammalian nuclei. *Nucleic Acids Res* 11, 1475–1489, doi:10.1093/nar/11.5.1475 (1983). [PubMed: 6828386]
75. Lu X. et al. MTA2/NuRD Regulates B Cell Development and Cooperates with OCA-B in Controlling the Pre-B to Immature B Cell Transition. *Cell Rep* 28, 472–485 e475, doi:10.1016/j.celrep.2019.06.029 (2019). [PubMed: 31291582]
76. McAlister GC et al. MultiNotch MS3 enables accurate, sensitive, and multiplexed detection of differential expression across cancer cell line proteomes. *Analytical chemistry* 86, 7150–7158, doi:10.1021/ac502040v (2014). [PubMed: 24927332]
77. Mellacheruvu D. et al. The CRAPome: a contaminant repository for affinity purification-mass spectrometry data. *Nat Methods* 10, 730–736, doi:10.1038/nmeth.2557 (2013). [PubMed: 23921808]
78. Olsen SN et al. MLL::AF9 degradation induces rapid changes in transcriptional elongation and subsequent loss of an active chromatin landscape. *Mol Cell*, doi:10.1016/j.molcel.2022.02.013 (2022).

79. Subramanian A. et al. Gene set enrichment analysis: a knowledge-based approach for interpreting genome-wide expression profiles. *Proc Natl Acad Sci U S A* 102, 15545–15550, doi:10.1073/pnas.0506580102 (2005). [PubMed: 16199517]
80. Mootha VK et al. PGC-1alpha-responsive genes involved in oxidative phosphorylation are coordinately downregulated in human diabetes. *Nat Genet* 34, 267–273, doi:10.1038/ng1180 (2003). [PubMed: 12808457]
81. Iniguez AB et al. Resistance to Epigenetic-Targeted Therapy Engenders Tumor Cell Vulnerabilities Associated with Enhancer Remodeling. *Cancer Cell* 34, 922–938 e927, doi:10.1016/j.ccell.2018.11.005 (2018). [PubMed: 30537514]
82. Dobin A. et al. STAR: ultrafast universal RNA-seq aligner. *Bioinformatics* 29, 15–21, doi:10.1093/bioinformatics/bts635 (2013). [PubMed: 23104886]
83. Li H. et al. The Sequence Alignment/Map format and SAMtools. *Bioinformatics* 25, 2078–2079, doi:10.1093/bioinformatics/btp352 (2009). [PubMed: 19505943]
84. Robinson JT et al. Integrative genomics viewer. *Nat Biotechnol* 29, 24–26, doi:10.1038/nbt.1754 (2011). [PubMed: 21221095]
85. Anders S, Pyl PT & Huber W. HTSeq--a Python framework to work with high-throughput sequencing data. *Bioinformatics* 31, 166–169, doi:10.1093/bioinformatics/btu638 (2015). [PubMed: 25260700]
86. Love MI, Huber W. & Anders S. Moderated estimation of fold change and dispersion for RNA-seq data with DESeq2. *Genome Biol* 15, 550, doi:10.1186/s13059-014-0550-8 (2014). [PubMed: 25516281]
87. Langmead B. & Salzberg SL Fast gapped-read alignment with Bowtie 2. *Nat Methods* 9, 357–359, doi:10.1038/nmeth.1923 (2012). [PubMed: 22388286]
88. Gu Z, Eils R. & Schlesner M. Complex heatmaps reveal patterns and correlations in multidimensional genomic data. *Bioinformatics* 32, 2847–2849, doi:10.1093/bioinformatics/btw313 (2016). [PubMed: 27207943]
89. Tange O. Gnu parallel-the command-line power tool.
90. Gao J. et al. Integrative analysis of complex cancer genomics and clinical profiles using the cBioPortal. *Sci Signal* 6, p11, doi:10.1126/scisignal.2004088 (2013).
91. David Wang XQ et al. Three-dimensional regulation of HOXA cluster genes by a cis-element in hematopoietic stem cell and leukemia. *bioRxiv*, 2020.2004.2016.017533, doi:10.1101/2020.04.16.017533 (2020).

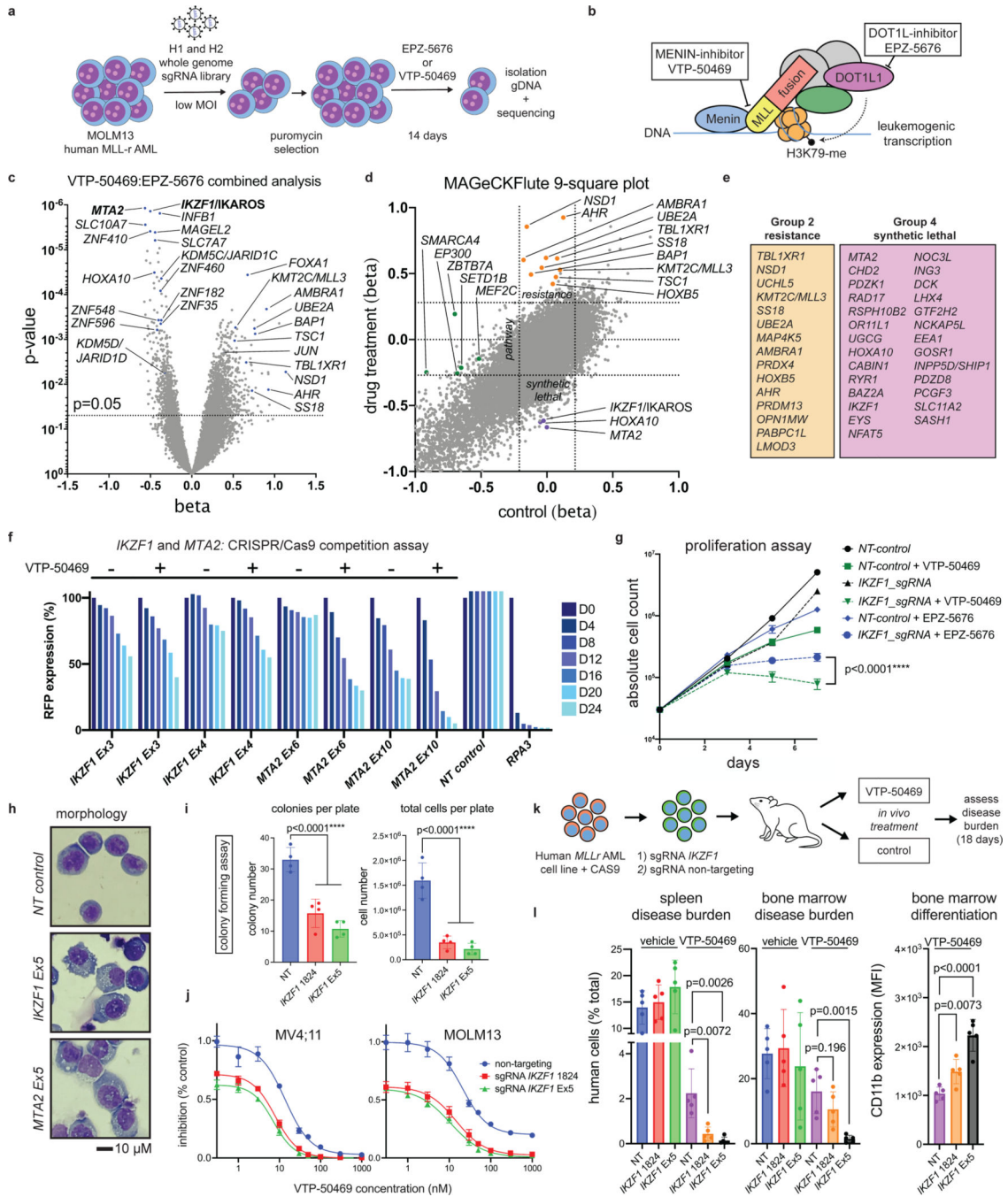


Figure 1. IKZF1/IKAROS and MTA2 exhibit synthetic lethal interaction with pharmacologic inhibition of MENIN and DOT1L.

a, Functional genetic screen schematic: cells treated with EPZ-5676 (1 μM), VTP-50469 (500 nM) or vehicle. **b**, Drug targeting of MENIN (VTP-50469) and DOT1L (EPZ-5676) disrupts MLL-fusion complex function. **c**, Volcano plot depicting Wald p-value and beta value calculated using MAGeCK MLE for the VTP-50469 and EPZ-5676 combined analysis comparing vehicle-treated (n=2) and drug-treated states (n=4) on Day 14. **d**, MAGeCKFlute 9-square correlation plot using the beta value calculated between Day 0 and Day 14

for vehicle-treatment as compared to drug treatment (VTP-50469 and EPZ-5676 screens combined). Regions corresponding to pathway (group1), resistance (group2) and synthetic lethal (group4) genetic hits are indicated. **e**, Leading edge analysis from GSEA showing overlapping genetic hits for each screen considered separately. **f**, CRISPR/Cas9-based competition assays targeting either *IKZF1* or *MTA2* monitoring *sgRNA*-RFP expression over time in Cas9-expressing MOLM13 AML cell line +/- VTP-50469. **g**, Proliferation assay on sorted, *sgRNA*-RFP-expressing cells +/- VTP-50469 or EPZ-5676. Data represent mean +/- SEM (n=3) with p-value calculated using paired, two-tail t-test. **h**, Cell morphology assessed using light microscopy (100X) 7 days following CRISPR/Cas9-mediated deletion of *IKZF1* or *MTA2*, compared to non-targeting sgRNA control **i**, Colony forming assay comparing MOLM13 cells with sgRNA targeting *Luciferase* (Non-Targeting) control versus two different sgRNAs targeting *IKZF1* (n =4 per sgRNA). Data represent mean +/- SEM. p-value determined by unpaired, two-tailed t-test. **j**, Proliferation assay comparing MOLM13 cells with sgRNA targeting *Luciferase* (NT control) and two sgRNAs targeting *IKZF1* (n=3 per sgRNA) upon treatment with VTP-50469 for 5 days. Data represent mean +/- SEM. **k**, Schematic for *in vivo*, MOLM13 xenograft experiment: 200,000 MOLM13 cells with sgRNA targeting *Luciferase* (NT control) versus two different sgRNAs targeting *IKZF1* (n = 5 per group) were injected via tail vein at Day 0, treatment began with VTP-50469 chow at Day 9, and mice were sacrificed at Day 18 when they became ill. **l**, MOLM13 xenograft experiment, burden of disease and differentiation markers in spleen and bone marrow after 9 days of VTP-50469 treatment. Data represent mean +/- SEM. p-value determined by unpaired, two-tailed t-test.

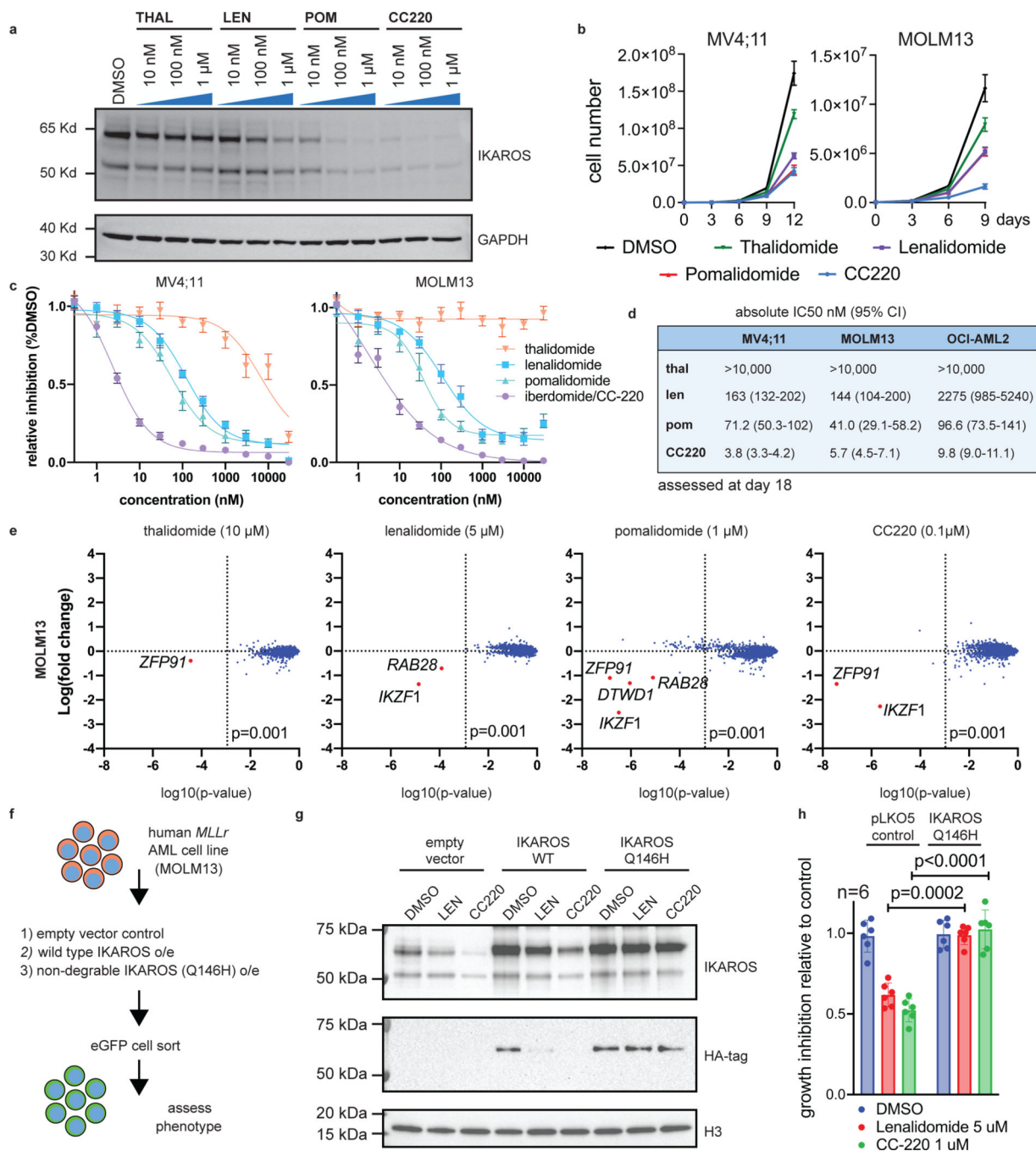


Figure 2. IMiDs effectively target IKAROS protein for degradation and show therapeutic efficacy in *MLL-r* AML.

a, Western blot analysis for IKAROS protein following treatment of the MOLM13 cell line for 5 h with increasing doses of THAL, LEN, POM and CC220, using GAPDH as a loading control. **b**, Proliferation assay measuring cell number over time for the MV4;11 and MOLM13 cell lines treated with vehicle-control (DMSO), THAL, LEN, POM and CC220. Data represent mean \pm SD (n=3). **c**, Dose response curves for MV4;11 and MOLM13 cell lines using THAL, LEN, POM and CC220. Data represent mean \pm SD

(n=6) with non-linear regression curve fit shown. Percentage indicated as a proportion. **d**, Calculated absolute IC50 and 95% confidence intervals for MOLM13, OCI-AML2 and MV4;11 AML cell lines, assessed by proliferation assay at Day 18. **e**, Scatterplot for MS determination of IMiD substrates 5 h after indicated drug treatment in the MOLM13 cell line. Data represent the Log-fold change in abundance and log10(p-value). p-value determined by moderated t-test as implemented by the Bioconductor Limma package. **f**, Schematic depicting generation of MOLM13 cell lines with IKAROS overexpression constructs treated with DMSO, LEN (5 uM), and CC220 (1 uM) for 5 hours. **g**, Western Blot showing IKAROS overexpression constructs, **h**, Proliferation assay showing rescue of antiproliferative effects with overexpressed, non-degradable IKAROS (Q146H). Data represent mean +/- SEM. p-value determined by paired, two-tail t-test.

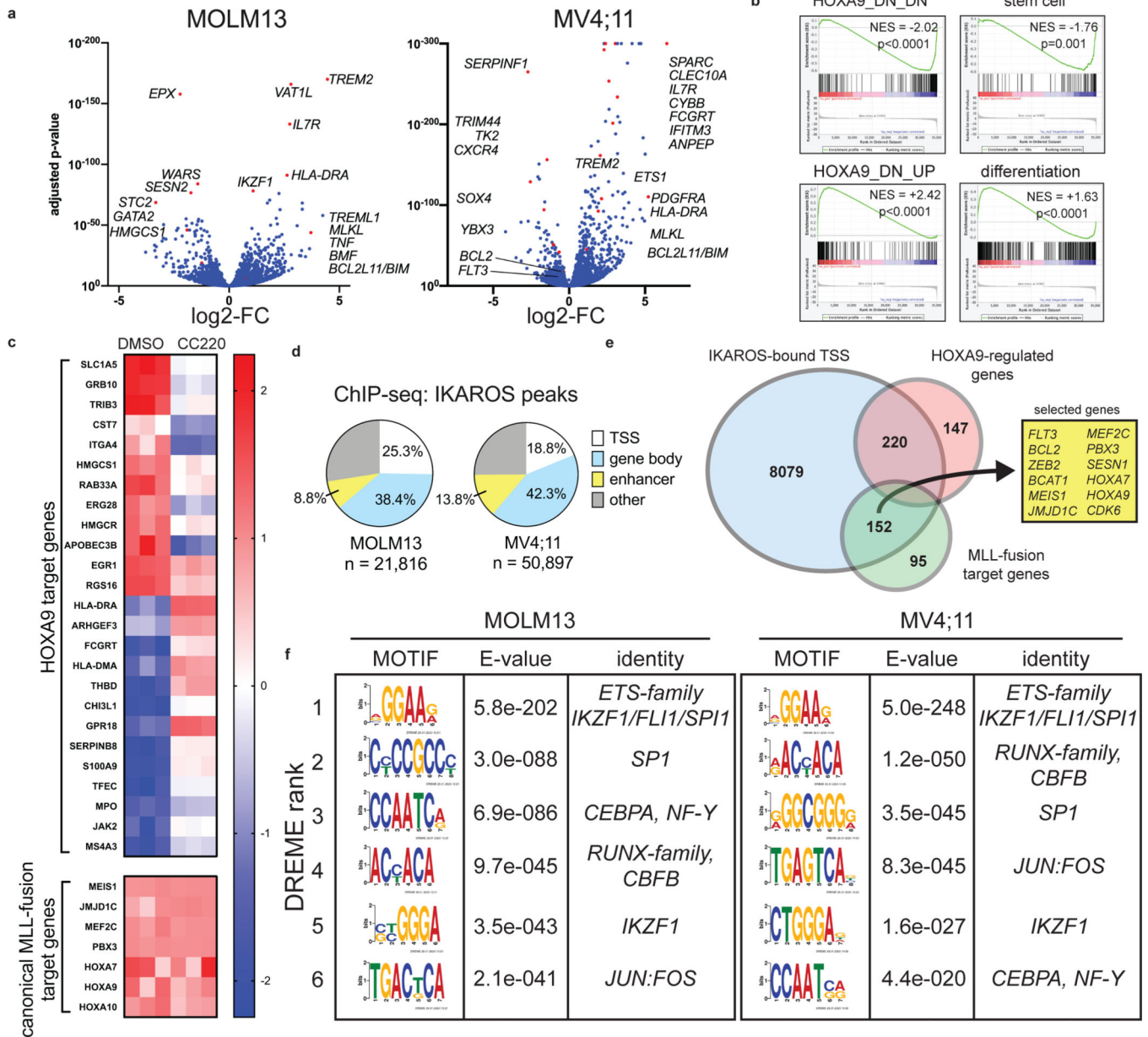


Figure 3. IKAROS is a core transcriptional regulator in *MLL-r* AML.

a, Volcano plots displaying RNA-seq data for MOLM13 (n=3) and MV4;11 (n=3) cell lines treated with iberdomide/CC220 1 μM for 3 days. Selected genes are indicated. **b**, Bar code plots depicting GSEA results for HOXA9-regulated genes, stem cell genes and myeloid differentiation in the MOLM13 cell line. Normalized enrichment score and family-wise error rate p-value determined by GSEA computational method. **c**, Heatmap depicting gene expression z-scores for canonical MLL1-fusion target genes and selected HOXA9-regulated genes following 3 days treatment with CC220 compared to DMSO-control in MOLM13 cell line. **d**, Percentage of ChIP-seq IKAROS peaks with 5-fold enrichment over background at regulatory regions, as indicated. **e**, Venn diagram depicting overlap between all TSS-proximal IKAROS peaks with genes within the MLL-fusion and HOXA/MEIS1 network.

f, CUT&RUN *de novo* DREME motif detection results for the MOLM13 and MV4;11 cell lines. Top 6 motifs detected for IKAROS, in order of statistical significance are shown. Motif, statistical E-value and predicted motif identity are indicated.

Author Manuscript

Author Manuscript

Author Manuscript

Author Manuscript

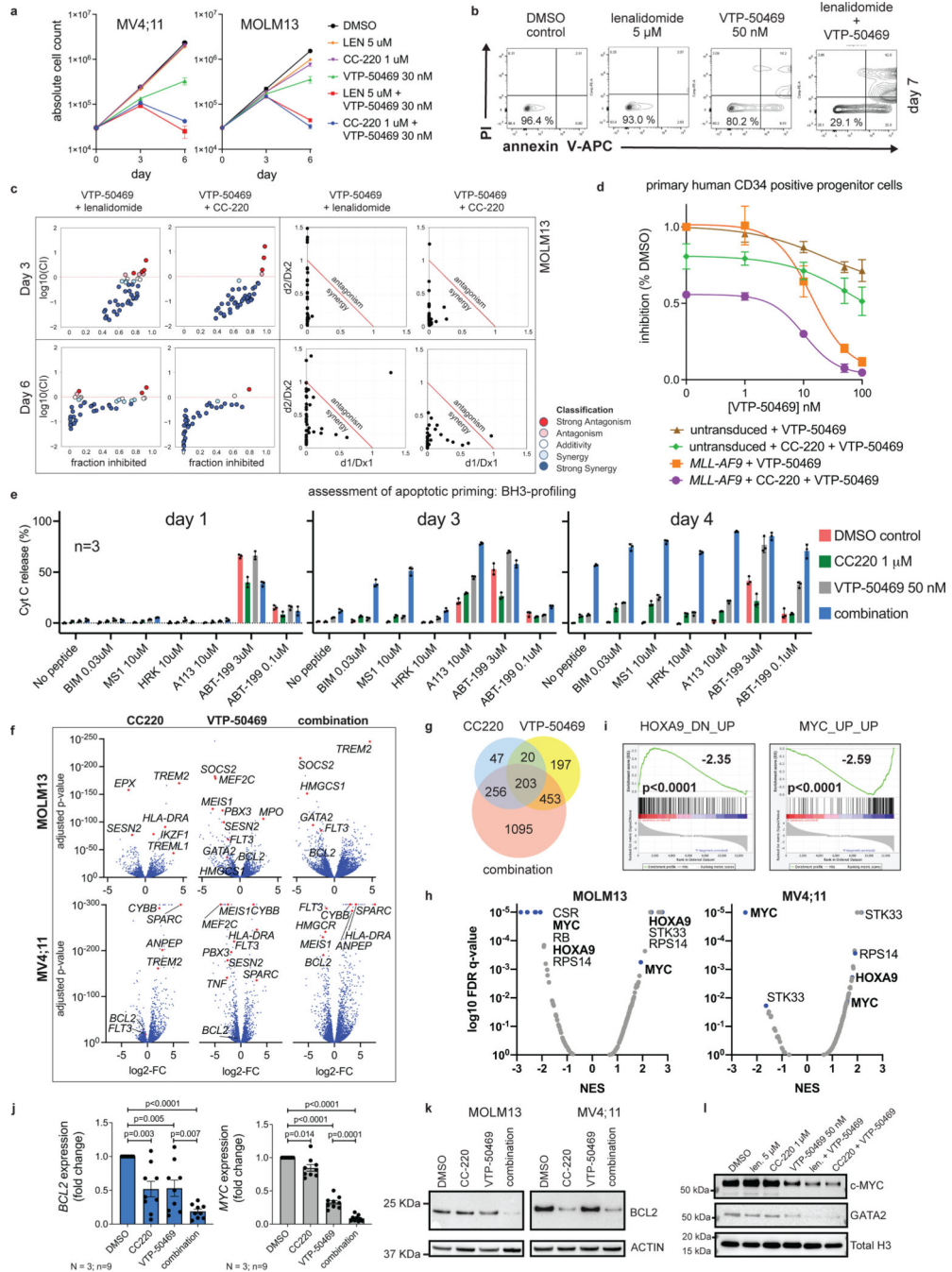


Figure 4. Combined targeting of MENIN and IKAROS results in synergistic induction of apoptosis and cooperative deregulation of gene expression.
a, Proliferation assay measuring cell number over time for the MV4;11 and MOLM13 cell lines following drug treatment. Data represent mean±SD (n=3). **b**, Analysis of annexin V staining (apoptosis) following drug treatment. Viable cell percentage indicated. Representative experiment shown. **c**, Proliferation assay in MOLM13 cells treated with VTP-50469 combined with either LEN or CC220. Synergy assessment by isobolograms (left) and Chou-Talalay (right) **d**, Proliferation assay after 6 day treatment in human CD34

progenitor cells that were non-transformed versus CD34 progenitor cells with *MLL-AF9* transformation. Data represent mean \pm SEM (n=3) relative to DMSO control. **e**, BH3-profiling in MOLM13 cells following drug treatments. Cytochrome C (Cyt C) release was measured. Data represent mean \pm SEM (n=3). **f**, Volcano plots displaying RNA-seq data for MOLM13 and MV4;11 cells following 3 days of drug treatment (n=3 per condition). **g**, Venn diagram for overlapping transcriptional changes between CC220, VTP-50469 and the combination (total number of genes indicated with >2-fold change and p-adj<0.05 as determined by DESeq2 package). **h**, GSEA results querying the *Broad* “oncogenic signatures” comparing combination treatment with VTP-50469 monotherapy. Results are displayed as dot plot of the log₁₀ false discovery rate (FDR) q-value and normalized enrichment score (NES). **i**, Bar code plots depicting selected GSEA results in MOLM13 cells from (h). Depicts additive effect of the combination compared to VTP-50469 therapy alone. Normalized enrichment score and family-wise error rate p-value determined by GSEA computational method. **j**, *BCL2* and *MYC* gene expression assessed by RT-qPCR following treatment with CC220 1 μ M, VTP-50469 250 nM and the combination. Data represent mean \pm SEM for combined analysis of 3 AML cell lines (MOLM13, MV4;11 and OCI-AML2) with n=3 replicates each (N=3; n=9). p-value determined by paired, two-tailed t-test. **k**, Western blot for BCL2 protein following treatment of MOLM13 and MV4;11 cells for 72 h with CC220 1 μ M, VTP-50469 50 nM and in combination, using ACTIN as a loading control. **l**, Western blot for MYC and GATA2 protein following drug treatment of MOLM13 cells for 72 hours. Histone H3 as a loading control.

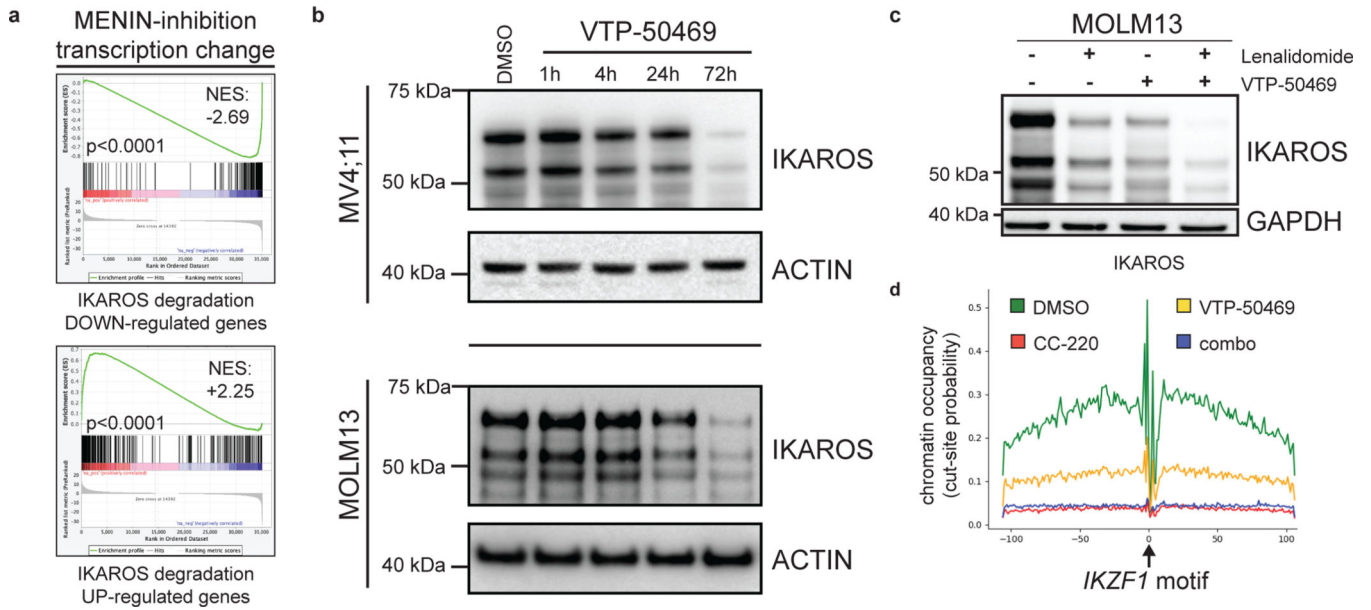


Figure 5. Inhibition of the MENIN-MLL1 protein-protein interaction leads to proteasomal degradation of IKAROS protein.

a, Bar code plots depicting the effect of MENIN-inhibition on the set of genes deregulated following IKAROS degradation by CC220 according to RNA-seq data on Day 3.

Normalized enrichment score and family-wise error rate p-value determined by the GSEA computational method.

b, Western blot analysis for IKAROS protein following treatment of the MV4;11 and MOLM13 cell lines for 1, 4, 24 and 72 hours, using ACTIN as a loading control.

c, Western blot analysis for IKAROS protein following treatment of MOLM13 human *MLL-r* AML cell line for 72 hours with LEN, VTP-50469 and in combination, using GAPDH as a loading control.

d, IKAROS protein chromatin binding at the *IKZF1* motif displayed as the cut-site probability ± 100 bp around the *IKZF1* motif under each drug treatment, as indicated.

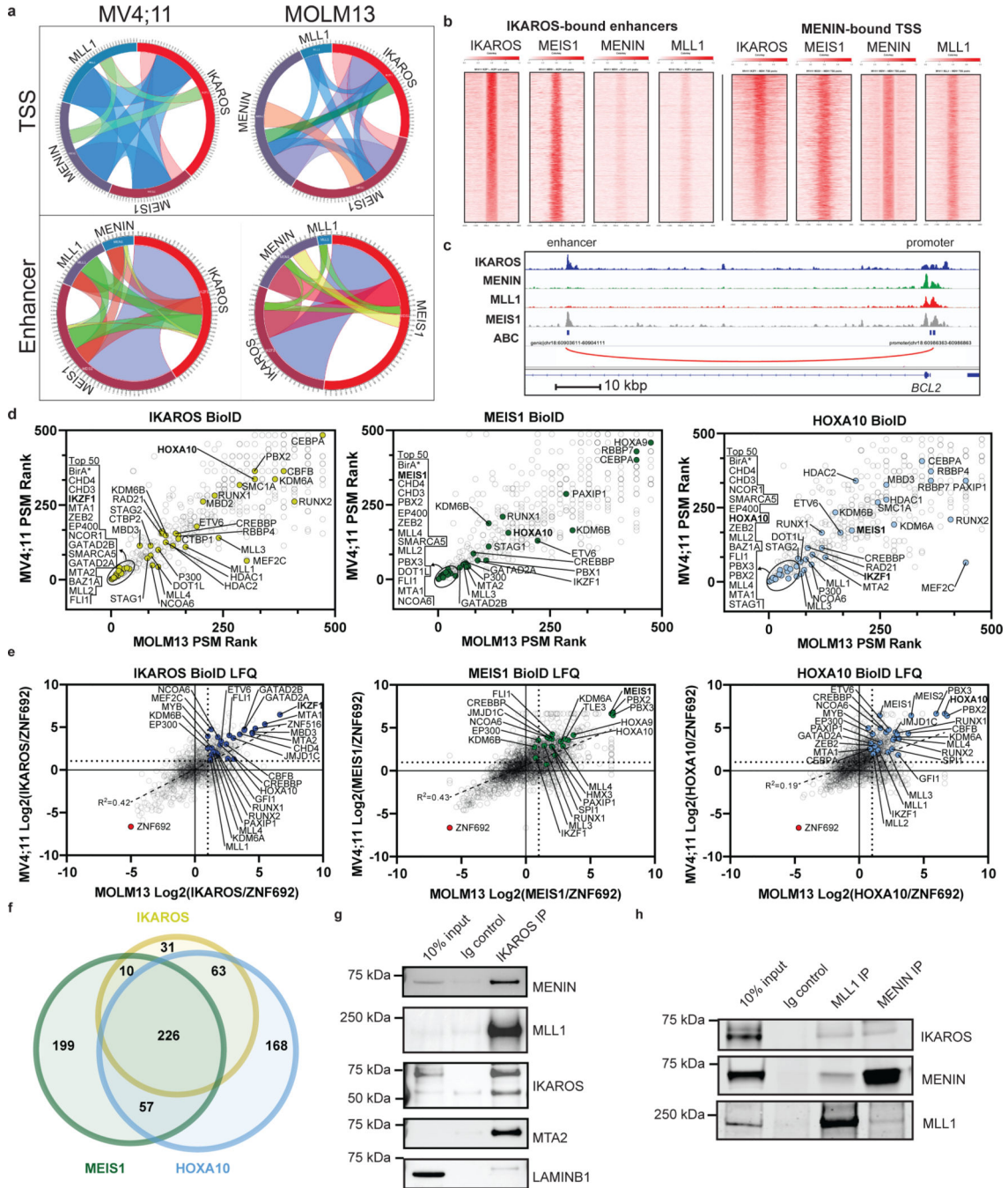


Figure 6. Chromatin co-occupancy and proximal protein-protein interactions of IKAROS and the MLL-fusion network.

a, Circos plots displaying co-occupancy between IKAROS, MEIS1, MENIN and MLL1 determined by ChIP-seq at all TSSes and active enhancers bound by at least one factor, genome wide. **b**, Tornado plots depicting chromatin occupancy as determined by ChIP-seq from the MOLM13 cell line at the indicated regulatory regions of interest: IKAROS-bound enhancers and MENIN-bound TSSes. **c**, IGV tracks depicting binding of IKAROS, MENIN, MLL1 and MEIS1 at the *BCL2* gene. The promoter and a selected intragenic enhancer

are indicated (genomic location indicated in Hg19). The predicted enhancer-promoter connection is indicated (red line). **d**, Dot plots displaying PSM rank values from spectral counting on proteins identified in IKAROS, MEIS1 and HOXA10 BioID in MV4;11 vs. MOLM13 cell lines by LC-MS/MS. Notable proteins ranked in the top 50 are circled and labelled on the left of each plot in order of lowest rank to highest (n=2). **e**, Dot plots displaying the Log_2 abundance ratios of IKAROS/ZNF692, MEIS1/ZNF692 and HOXA10/ZNF692 BioID in MV4;11 vs. MOLM13 cell lines derived from label free quantitation analysis of LC-MS/MS data (n=2). **f**, Venn diagram displaying the number of proteins identified in label free quantitation analysis of the MV4;11 IKAROS, MEIS1 and HOXA10 BioID LC-MS/MS data. All proteins included in Venn diagram have a >2-fold enrichment over the ZNF692 control. **g**, Direct protein Co-IP using IKAROS as the bait and probed for MLL1, MENIN, MEIS1, MTA2 and LAMINB1 for a negative control, in the MV4;11 cell line. **h**, Direct protein Co-IP using MLL1 and MENIN as the bait and probed for MENIN, MLL1 and IKAROS, in the MV4;11 cell line.

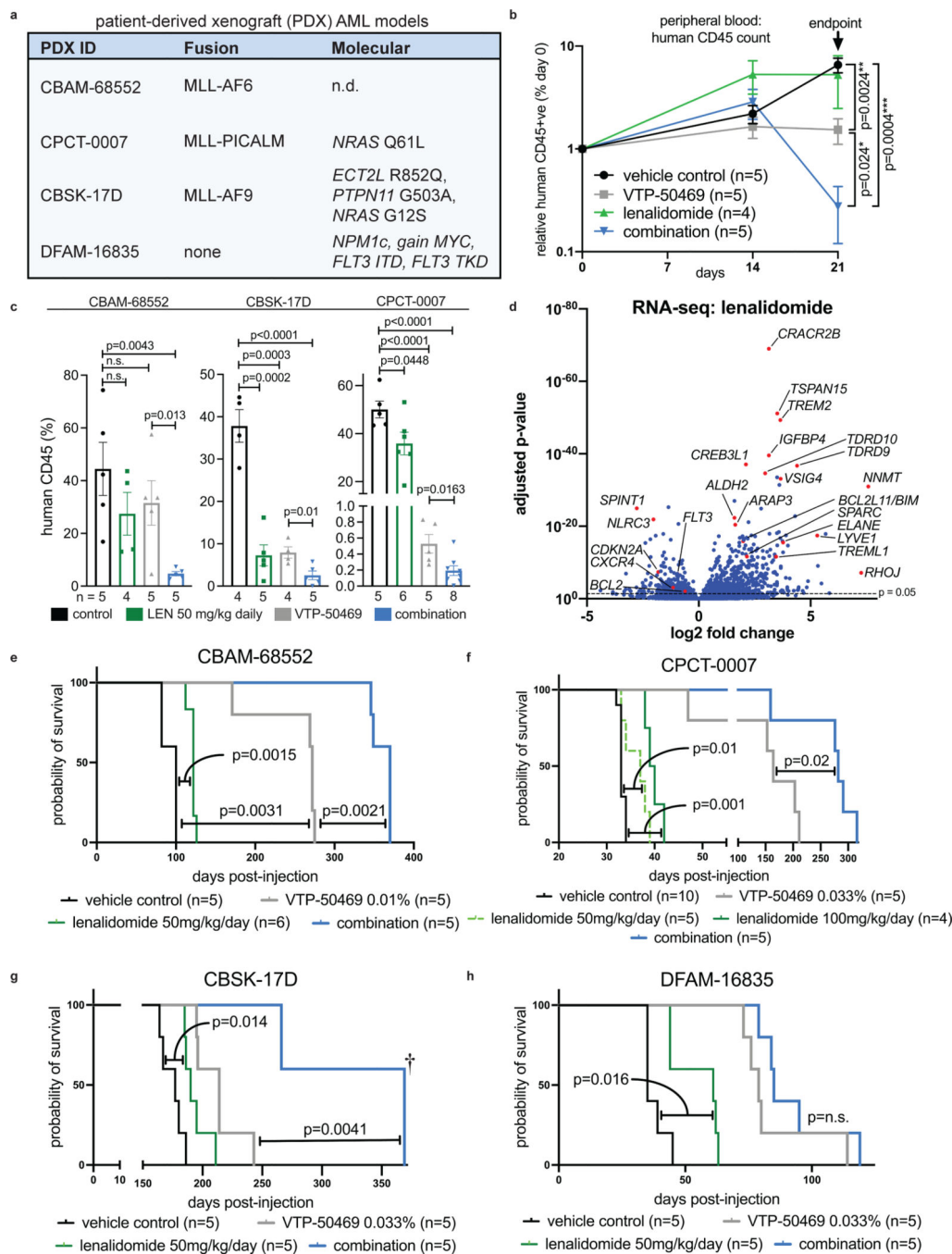


Figure 7. Combination therapy with VTP-50469 and LEN results in synergistic anti-leukemic activity *in vivo*.

a, Four PDX models used indicating PDX identification number (ID), MLL-fusion present and additional molecular features. **b**, Peripheral blood circulating human leukaemia cells indicated by human CD45 positive cells using flow cytometry during treatment with vehicle, LEN 50 mg/kg daily, VTP-50469 continuously and the drug combination in CBAM-68552. Data represent mean \pm SEM with pair-wise p-value calculated using the two-tail t-test. **c**, Analysis of bone marrow from transplanted mice following 3 weeks

(CBAM-68552), 2 weeks (CBSK-17D) or 1 week (CPCT-0007) of drug treatment for leukaemia burden (human CD45 +ve), as assessed by flow cytometry. Data represent mean \pm SEM with p-value calculated using the two-tail t-test (n=4–5 mice in each group). **d**, Volcano plot depicting RNA-seq results from human leukaemia cells isolated from CBAM-68552 mouse bone marrow following *in vivo* treatment with LEN (n=4) compared to vehicle control (n=5). Selected genes are indicated. **e**, Kaplan-Meier Survival curves for CBAM-68552 following 4 weeks treatment with vehicle, LEN 50 mg/kg/day, VTP-50469 0.1% continuously; p-value by Log-Rank (Mantel-Cox) test. **f**, Kaplan-Meier Survival curves for CPCT-0007 following 2 weeks treatment with vehicle, LEN 50 mg/kg/day, LEN 100 mg/kg/day, VTP-50469 0.033% continuously, or the combination of LEN 50 mg/kg/day with VTP-50469 0.033%; p-value by Log-Rank (Mantel-Cox) test. **g**, Kaplan-Meier Survival curves for CBSK-17D following 2 weeks treatment with vehicle, LEN 50 mg/kg/day, VTP-50469 0.033% continuously; p-value by Log-Rank (Mantel-Cox) test. 3 combination-treated mice were sacrificed after 350 days without evidence for leukemia by flow cytometry of bone marrow (\dagger) **h**, Kaplan-Meier Survival curves for DFAM-16835 following 2 weeks treatment with vehicle, LEN 50 mg/kg/day, VTP-50469 0.033% continuously; p-value by Log-Rank (Mantel-Cox) test.